In-situ measurements of the Liquid-Phase Sintering of Zinc Oxide

Von der Fakultät für Biologie, Chemie und Geowissenschaften

Der Universität Bayreuth

zur Erlangung der Würde eines Doktors der Naturwissenschaften

- Dr. rer. nat. -

Genehmigte Dissertation

vorgelegt von
Mohammad Lutful Arefin
(M.Sc. Advanced Materials)
Aus Bangladesch

Bayreuth, May 2009

Copyright waiver

I hereby declare that this submission is my own work and that, to the best of my knowledge and belief, it contains no materials previously published or written by another person nor material which to a substantial extent has been accepted for the award of any other degree or diploma of the university or other institute of higher learning, except where due acknowledgement has been made in the text.

.....
Signature
Mohammad Lutful Arefin

Board of examiners
Prof. Josef Breu, University of Bayreuth
Prof. Gerd Müller, Fraunhofer Institute for Silicate Research
Prof. Hans Keppler, University of Bayreuth
Prof. Jürgen Senker, University of Bayreuth

.....
Date of submission:

Acknowledgements

It's certainly a great pleasure to have this opportunity to express my heartiest gratitude to those people who have been a source of ample help in various ways during my completion of this work. At first, I must convey my appreciation and gratitude to Dr. Friedrich Raether who has supervised my entire work closely and extended his untiring support all the time at the Fraunhofer Institute for Silicate Research (ISC), Würzburg, Germany.

As the fellow of this research work I am highly grateful to Prof. Josef Breu of University of Bayreuth, Germany, Prof. Gerd Müller of Fraunhofer ISC, Germany and Mr. Felix Greuter of ABB, Switzerland for their valuable advices and suggestions on many issues which may have not been addressed unless their careful notification and suggestions.

Not to mention that I am very much grateful to the *Elitenetzwerk, Bayern* (ENB) for their funding to carry out the research work and to the administration of Bayerisches Geoinstitut for their support and coordination of enormous facilities and academic activities throughout my work.

My family has been a great source of inspiration for the successful completion of this work. Without this inspiration the work would be as difficult as it would be without the supports of the aforementioned persons.

Last but not the least, I feel deeply acknowledged to my friends, colleagues, technicians who have been sources of great assistance and inspiration over the entire term.

I remain,

Md. Lutful Arefin

Würzburg, March 2009

… … … … to our unborn child

Table of Contents

Zusammenfassung

Polykristalline Keramiken, die aus halbleitendem ZnO und verschiedenen Additiven bestehen, zeigen – ähnlich wie Zener-Dioden - eine stark nichtlineare Strom-Spannungs-Kennlinie. Die daraus hergestellten Bauteile wirken bis zu einer bestimmten Durchbruchfeldstärke (E_{BR}) als elektrischer Widerstand und zeigen eine hohe Stromleitfähigkeit unmittelbar darüber. Außerhalb der Durchbruchfeldstärke ist die Kennlinie linear. Diese spezielle Kennlinie und die Stabilität gegenüber wiederholten Belastungen oberhalb E_{BR} haben dazu geführt, dass Metalloxidvaristoren heute vielfach zur Spannungsbegrenzung in elektrischen Schaltkreisen verwendet werden.

ZnO, das mit Bi_2O_3 und Sb_2O_3 (ZBS) dotiert ist, ist das Basismaterial für keramische Varistoren. Die Phasenumwandlungen während der Sinterung von ZBS wurden mit Synchrotronstrahlung an 1 mm dicken Proben untersucht. Mithilfe thermodynamischer Berechnungen wurden Phasenumwandlungen, die Stabilität der Additivoxide und der Einfluss der Sauerstofffugazität auf die Sinterung erklärt. Sb_2O_4, Pyrochlor, Trirutil und Spinell bildeten sich im Temperaturbereich von 500°C bis 800°C. Die Oxidation von Antimon wurde durch den Sauerstoffpartialdruck kontrolliert. Sie bestimmte sowohl die Phasenbildung als auch die Sinterkinetik im ZBS-System. Die Mikrostruktur der gesinterten ZBS-Keramiken wurde durch drei Phasen bestimmt: ZnO, Pyrochlor und Spinell. Die Kenntnis der Entwicklung dieser Phasen in Abhängigkeit von Temperatur und Zeit trägt wesentlich zum Verständnis der Grundfunktion des ZnO-Varistor-Systems bei.

Die Kinetik der Flüssigphasensinterung im System $ZnO\text{-}Bi_2O_3\text{-}Sb_2O_3$ wurde mit einem optischen Dilatometer unter Verwendung geschlossener Tiegel untersucht. Die Kinetik Field-Methode wurde modifiziert, um Sinterraten mit Modellen zum Flüssigphasensintern

vergleichen zu können. Informationen zum Kornwachstum wurden direkt dem Kinetic Field-Diagramm entnommen und mit Mikrostrukturanalysen an abgeschreckten Proben verglichen. Zwischen beiden Methoden wurde eine akzeptable Übereinstimmung erreicht, was zeigt, dass die modifizierte Kinetic Field-Technik als ein effizientes Werkzeug zur Prozessoptimierung eingesetzt werden kann.

Summary

Polycrystalline ceramic semiconductor devices based on ZnO and several additive oxides show highly non-ohmic current-voltage behavior similar to the Zener diodes. The devices act as an insulator up to a certain electrical field called the breakdown field (E_{BR}) but change into a highly conducting one just above it. Below and above the breakdown field they behave perfectly ohmic. This overall non-linear current-voltage characteristic together with the ability to withstand repeated high power pulses has made metal oxide varistors popular as "surge-arrestors" in electrical circuitry.

ZnO doped with Bi_2O_3 and Sb_2O_3 (ZBS), is the basic system for ceramic varistors. Phase formation during sintering of ZBS was measured in situ, using 1 mm thick samples and synchrotron X-rays. Thermodynamic calculations were performed to explain phase formation, composition, stability of additive oxides and influence of the oxygen fugacity on sintering. Sb_2O_4, pyrochlore, trirutile and spinel were formed at temperatures of 500°C to 800°C. The oxidation of antimony was controlled by the oxygen partial pressure and affected both, phase formation and sintering kinetics, in the ZBS system. There are three well defined phases in the final microstructure e.g. the ZnO-grains, Pyrochlore and Spinel phases. The evolution of these phases with temperature and time are important facts to the understanding of the basic functionality of the ZnO varistor system.

Liquid phase sintering kinetics in the system ZnO-Bi_2O_3-Sb_2O_3 was studied using closed crucibles and an optical dilatometer. The kinetic field technique was modified to compare densification rates with liquid phase sintering models. Grain growths data were derived directly from the kinetic field diagram and compared to microstructure analysis of quenched samples. A reasonable agreement was obtained between both techniques – demonstrating that the modified kinetic field technique is an efficient tool for process optimization.

Chapter 1: Introduction

1.1 Electrical characteristics of varistors

AC voltage (or current) is represented by sinusoidal wave function (see figure 1.1) as $v = v_p \cdot sin(2\pi \cdot f \cdot t)$ where, v_p is the maximum or peak voltage in volt, f is the frequency in Hz (or sec^{-1}) and t is time in second. In European standard, the supply current has a peak of 220 V and frequency is 50 hz.

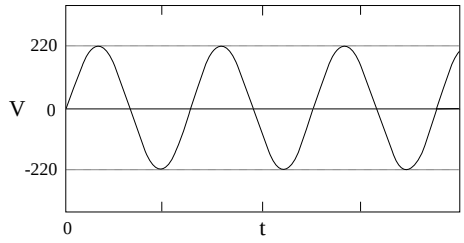

Figure 1.1: Wave form of standard voltage from an AC source as function of time

Unfortunately, although the suppliers always try to maintain a steady voltage level over time, it is more realistic to have some unexpected over- and/or under –shoots of the peak voltage (see figure 1.2).

Figure 1.2 shows a typical upsurge in a 120 V_{rms} (root mean squared) supply which is normally caused from a sudden load decrease or even the turning off of high power electrical equipment. This swell in voltage can be very harmful for electrical appliances in the household as well as industries. Surges of other kinds can be caused by lightning (indirect surge) and switching of power transmission lines.

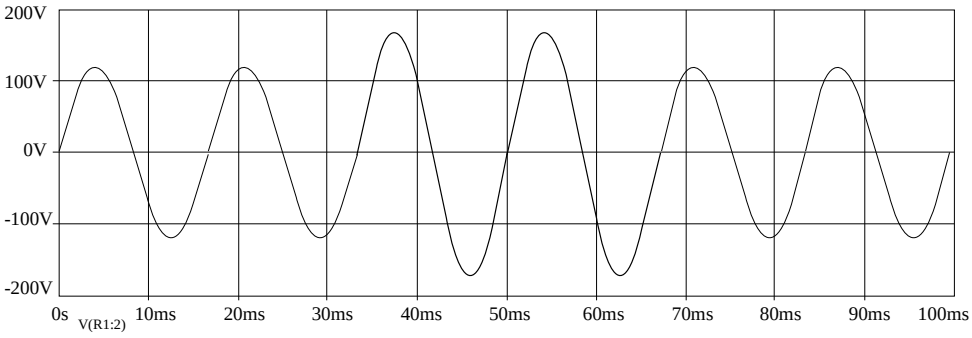

Figure 1.2: Typical upsurge experienced by a standard supply of 120 V_{rms}

The devices that protect electrical equipments from such surges are generally called surge arrestors. The special types of surge arrestors which limit the voltage-surge by their non-linear impedance characteristics are called varistors. Zinc Oxide is used as basis material in metal-oxide varistors (MOV) which has a high value of non-linear coefficient (compare figure 1.3) represented by alpha (α). The definition of the non-linear coefficient alpha is given by the following equation,

$$I = K \cdot V^{\alpha} \qquad (1.1)$$

where I is the current, K is a constant and V is the voltage. For metal oxide varistors the value of alpha can be very high and commercial varistors have alpha values as high as 50 to 80 or even higher.

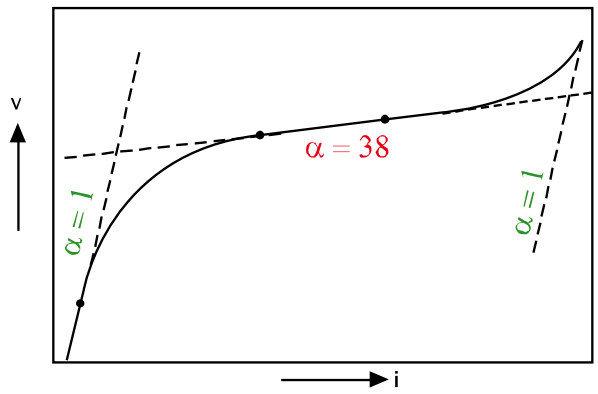

Figure 1.3: Non linearity in ZnO-based varistor ceramics

1.2 ZnO-based varistor ceramics

Zinc Oxide based varistors act as an insulator up to a certain electrical field called the breakdown field (E_{BR}) but change into a highly conducting state just above it. As shown in figure 1.3 – below and above the breakdown they behave perfectly ohmic. This overall non-linear current-voltage characteristic together with the ability to withstand repeated high power pulses has made this metal-oxide varistor popular as "surge-arrestors" in electrical circuitry where they protect the wiring by rapidly discharging transient current surges and hence limiting the potential difference across the device.

Zinc Oxide based varistors are the classical grain-boundary-active electronic ceramic devices in which the varistor functionality is essentially resulted from the electronic states of the dielectric grain boundary layer [1]. Since the early seventies, when it was first reported by Matsuoka [2], ZnO has become the most popular industrial ceramic for metal oxide varistor (MOV) fabrication. The exceptional current-voltage behaviour of ZnO varistors was attributed mainly to the presence of the numerous oxides which segregate at the ZnO-grain boundaries. These additive-oxides are categorized in three main groups – the varistor-action oxides, specific current-voltage modifiers and spinel forming grain-growth inhibitors. Bi_2O_3, being the varistor-action oxide, forms the liquid through a eutectic melting with ZnO at 738°C [3] which promotes densification and enables liquid phase sintering. During cooling it forms tunnel barriers at the ZnO grain boundaries and this leads to the non-ohmic behaviour [4]. Sb_2O_3, on the other hand, is the spinel forming grain-growth inhibitor which produces an orthorhombic spinel ($Zn_7Sb_2O_{12}$) [5,6].

Equation 1.2 gives a relation between the microstructure of the varistor and the breakdown field Ev at which the switching in varistor from linear to extreme non-linearity takes place.

$$E_v = V_{gb} \cdot N_g \qquad (1.2)$$

where, E_v is the breakdown voltage, V_{gb} voltage per intergranular boundary and N_g is the number of grains per unit thickness across the varistor. Figure 1.4 shows the microvaristors which are comprised of two adjacent grains of ZnO and such microvaristors in series give the total varistor effect. It has also been shown that V_{gb} is almost independent of the composition of the varistor [7] and typically has a value of 3.0 – 3.6 V [8].

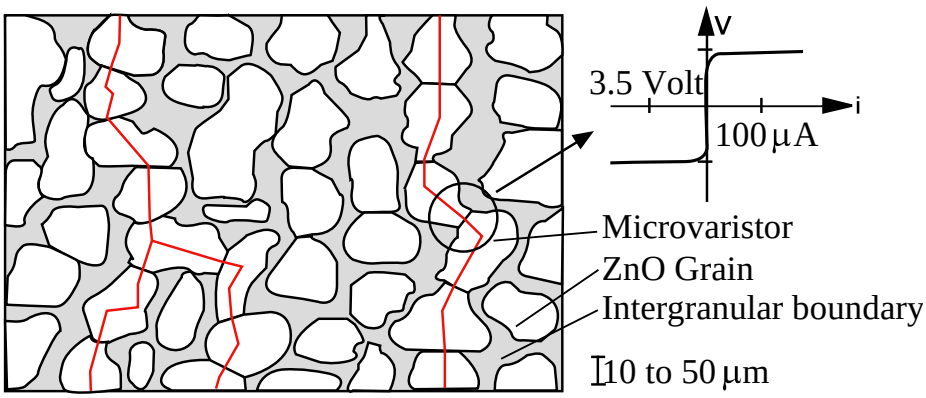

Figure 1.4: Non-linearity at grain boundaries of ZnO varistor ceramics producing the total varistor effect in ceramics

From this simplified equation one could argue that a 1 mm thick varistor with 10 µm average grain size will exhibit a breakdown voltage of 300 Volts. However, one has to bear in mind that for a wider grain size distribution the electrical pathway could be dictated by the larger grains. So, the breakdown voltage is not representative of the average grain size in such cases. Apart from this controversy in the perceptions of the device-physics of varistors, it has generally been agreed that varistor functionality in MOV's result from Schottky barriers formed at the grain boundaries [4,9].

1.2.1 Studies on ZBS varistors

Many researchers studied this ZBS (ZnO-Bi_2O_3-Sb_2O_3) ceramic system for its importance in the varistor industry. Matsuoka studied sintering temperature, and additive content of ZnO varistor ceramic composed of five additives e.g. Bi_2O_3, CoO, MnO, Cr_2O_3 and Sb_2O_3. Segregation layers of additive oxides along ZnO-grain boundaries which were held responsible for the non-ohmic properties were detected by electron microscopy and x-ray analysis.

Three years after Matsuokas finding, Joe Wong [10] investigated a complex multicomponent varistor system based on ZnO and small additions of Sb_2O_3, Bi_2O_3, Co_2O_3, MnO_2 and Sn_2O_3. It was reported that spinel works as a grain growth inhibitor and retards the growth of ZnO grains during sintering. A $Bi_2Zn_{4/3}Sb_{2/3}O_6$ pyrochlore phase was found to form a three-dimensional thread like network indicating a liquid phase at high temperature. These phases were discussed as function of temperature and equilibrium composition which suggested that dissociation of pyrochlore at higher temperature could give additional spinel and liquid Bi_2O_3. Electrical behaviour of the varistor was attributed to the network of ZnO-pyrochlore junctions.

Masanory Inada [11] came up with the detailed crystal structures of the main constituent-phases of such varistor ceramics in the middle of 1977 which was a milestone in ZnO-based varistor-studies so far. He studied the formulations of commercial ZnO ceramic with Bi_2O_3, Sb_2O_3, Co_2O_3, MnO_2 and Cr_2O_3 as additives. The phases found were described as functions of additive amount and sintering temperature. There were majority ZnO phases dissolving Mn and Co components, spinel phases of $Zn_7Sb_2O_{12}$ dissolving Cr, Co and Mn components, Bi-rich phases with variety of compositions and morphologies. All these phases and their formation were discussed in terms of temperature and additive content of the basic system.

Several other works followed in studying microstructural aspects of ZnO varistors [4, 11, 5, 12, 13]. E.R. Leite tried to formulate a reliable chemical pathway for the formation of important phases like spinel and pyrochlore where he suggested the following sequence of reactions during liquid phase sintering of ZnO ceramics:

At 527°C,

$$Sb_2O_3(s) + O_2 \rightarrow Sb_2O_5(l) \quad (1.3)$$

At 700-800°C,

$$Sb_2O_5(l) + ZnO(s) \rightarrow ZnSb_2O_6(s) \quad (1.4)$$

At >800°C,

$$ZnSb_2O_6(s) + 6ZnO(s) \rightarrow Zn_7Sb_2O_{12}(s) \quad (1.5)$$

Between 700- and 900°C,

$$3ZnSb_2O_6(s) + 3Bi_2O_3(s) + ZnO(s) \rightarrow 2Zn_2Bi_3Sb_3O_{14}(s) \quad (1.6)$$

The pyrochlore phase is formed at temperatures between 700°C and 900°C (see equation 1.6 above). It had an impact on densification kinetics [14]. The spinel phase inhibits grain growth of the ZnO grains and retards densification [12].

While some groups continued their investigation at the microstructural level to know more about the individual phases, their formation mechanism, structures and morphology, other groups started to investigate the role of the additives on the varistor properties.

1.2.2 Role of dopants

It is clear from the foregoing chapters that Zinc Oxide intrinsically has this exceptional current-voltage characteristic but may not be able to

produce varistor effect without dopants. The varistor functionality largely depends on the chemical compositions and density of the grain boundaries [14]. With very large grain sizes the effective number of grain boundaries is reduced and with very low impurity content the varistor may show more linear I-V curves which is not expected for a surge-arrestor. Clarke [4] describes the varistor behaviour to be depending on few prerequisites – an intervening grain boundary layer, good dewettability of the ZnO by liquid phase during cooling down and electronic defect states that must be inherited by the barrier layer. The behaviour of the intergranular regions is often modelled as a double Schottky barrier (DSB), with the additives to be represented as bulk or interfacial defect states.

Although commercial varistors may have as many as 15 different additive oxides making it difficult to estimate functions of each individual dopant, we can concentrate only on Bi_2O_3 and Sb_2O_3 in this discussion keeping the foregoing prerequisites for varistor functionality in mind.

Besides Bi_2O_3, Sb_2O_3 also plays important roles in varistor functionality. This dopant creates a pyrochlore phase ($Zn_2Bi_3Sb_3O_{14}$) with the other two constituents at very low temperature (~600°C) which later decomposes into a spinel phase ($Zn_7Sb_2O_{12}$) above 900°C by reacting with ZnO [11]. The growth of ZnO grains has found to be inhibited by spinel grains which act as anchor/pinning points and ceases the grain boundary migration of ZnO [14]. However, the pyrochlore phase was also reported to be inhibiting the ZnO-grain growth [17].

Effects of the additive oxides were studied in great details by Kim et al [13]. Effects of Sb_2O_3 on densification of pure ZnO was studied and compared with that of other additives such as $ZnSb_2O_6$, α-$Zn_7Sb_2O_{12}$, and Sb_2O_4. It was found that densification temperature is higher than

that of pure ZnO when Sb_2O_3 is added at up to 2 mol%. This was explained by the volatile nature of Sb_2O_3 so that Sb_2O_3 evaporates during oxidation at about 500°C and condenses on ZnO particle surfaces as a non-crystalline phase with an unknown composition. This hinders the materials transport across ZnO particles and thereby retards densification.

In a different work Kim et al [18] showed how densification is related to the pyrochlore formation and so to the ratio of Sb/Bi rather than the absolute amount of Sb_2O_3 and Bi_2O_3 additives. It was shown that the liquid forms at about 750°C for Sb/Bi<1 and at about 1000°C for Sb/Bi >1 by the reaction of pyrochlore phase with ZnO.

The effect of Bismuth Oxide content on the sintering of ZnO was also studied by Kim et al [19] showing that a small amount of Bi_2O_3 in ZnO ((≤0.1 mol%) retards the densification but an amount higher than 0.5mol% promotes it. The effect was attributed to the grain boundary mobility which increases by liquid formation.

Lao et al [20] studied the effect of Bi_2O_3 and Bi_2O_3+Sb_2O_3 additions on the size distribution of ZnO grains and reported that without the usage of a powder bed the addition of Bi_2O_3 provides a transient liquid phase that enhances the densification. It was also observed that the residual Bi alters the surface/grain boundary energy ratio, which encourages the ZnO grains to grow. They could show that the addition of both Bi_2O_3 and Sb_2O_3 induces the formation of pyrochlore, spinel and inversion boundaries. Their presence reduces not only the average grain size, but also the size variation.

Some works have been done in thermodynamic aspects particularly aiming at the understanding of the sintering of ZnO and/or influence of additives on the sintering. More specific thermodynamic studies are done between 1998 and 2006 [21-26].

High-resolution transmission electron microscopy (HRTEM) and scanning transmission electron microscopy (STEM) was used by Wang et al [22] to analyse the equilibrium configuration of Bi-doped ZnO grain boundaries. A nanometer-thick amorphous film was reported to be found along the ZnO-grains. Three different routes were used to reach this phase - samples were cooled from above the eutectic temperature ($T_{eutectic}$ = 740°C), processed entirely below the eutectic temperature, and desegregated by high applied pressure (1 GPa) followed by annealing at ambient pressure to restore segregation. In all cases the existence of such amorphous film was ensured and the electronic characteristics of this film were discussed.
Asryan et al [24] did important observations on the stability of Antimony Oxide by Knudsen Effusion method with mass spectrometric analysis of the gas phase for Antimony Oxide and found that Sb_2O_3 does not sublime congruently but incongruently. This group also calculated the enthalpies of formation of Sb_4O_6(g), Sb_2O_4(s) and Sb_6O_{13}.

Two groups [25,26] studied the phase equilibria relations in the binary system Bi_2O_3-ZnO. Guha et al [25] used quenching technique to study the binary system. Two new phases α-Bi_2O_3 and $Bi_{38}ZnO_{58}$ were observed to decompose from body-centered cubic solid solution γ-Bi_2O_3 below the eutectic temperature (740°C) on cooling the heat treated samples. The compound $Bi_{38}ZnO_{58}$ has a crystal structure analogous to the body-centred cubic γ-Bi_2O_3 solid solution and melts incongruently at a temperature near 753 ± 2°C to yield γ-Bi_2O_3 and liquid. A binary eutectic occurs between $Bi_{38}ZnO_{58}$ and ZnO at a composition near 25 ± 1.0 mol% ZnO with a melting temperature of 738 ± 2°C. Based on the data obtained in this study, they also proposed a revised phase diagram of the binary system Bi_2O_3-ZnO.

The other group [26] actually investigated the Bi_2O_3-rich regions of the binary Bi_2O_3-ZnO system. This study was conducted using CALPHAD

methodology (CALculation of PHAse Diagrams), using the software Thermo-Calc. An optimal set of thermodynamic functions for the binary was obtained and compared. The comparison showed good agreement between experimental data and calculations. The thermodynamic study also reported the existence of a $19Bi_2O_3.ZnO$ compound as well as that of the δ-Bi_2O_3 and reported them to occur in the Bi_2O_3-rich regions of the ZnO-Bi_2O_3 system.

1.3 Liquid Phase Sintering

1.3.1 Stages and features of liquid-phase sintering

The dominant stages of liquid phase sintering have been identified (compare figure1. 5) as following,

- Redistribution of the liquid and rearrangement of the particulate solid under the influence of capillary stresses
- Densification and grain growth by solution-reprecipitation and
- Final-stage sintering dominated by Ostwald ripening or coarsening.

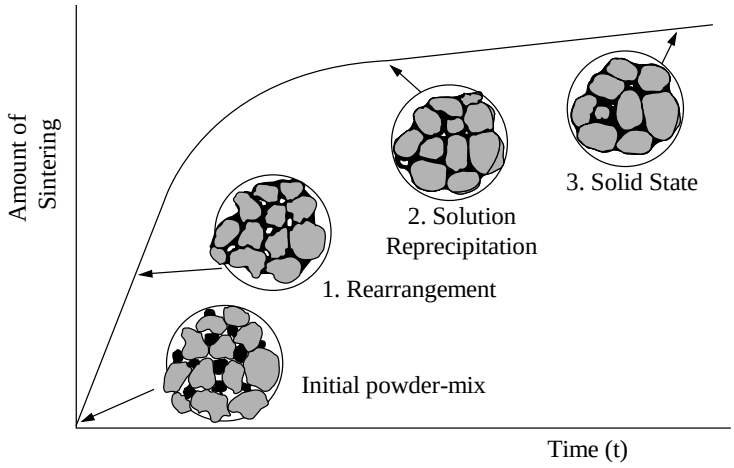

Figure 1.5: Schematic evolution of a powder compact during liquid-phase sintering (redrawn from Rahaman [27])

After melting reduction of friction between the solid-solid contacts occurs due to the interlaying liquid-bridge which the liquid phase creates by wetting and spreading over the solid surfaces. This can be shown using the idealized two-sphere model [27] as seen in figure 1.6.

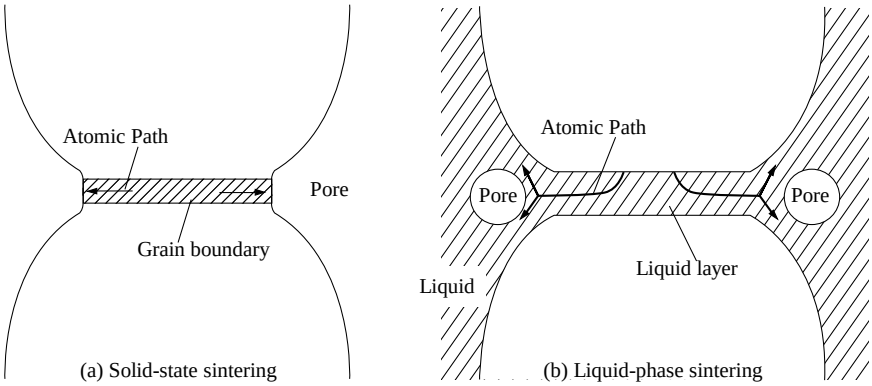

Figure 1.6: Idealized two-sphere model to compare microstructural aspects of (a) solid-state and (b) liquid-phase sintering (redrawn from Rahaman [27])

In the presence of such an interlaying liquid-layer the solid can rearrange more easily under the influence of a capillary force exerted by the liquid and densification can then proceed at an enhanced rate. The driving force for such mass transport can be assumed to come from the fact that the system always tries to reduce the liquid-vapour interface between pores and liquid.

After the formation of the eutectic liquid, three different kinds of interfaces coexist – solid-vapour (γ_{sv}), solid-liquid (γ_{sl}) and liquid-vapour (γ_{lv}). By balancing the horizontal components of the vectors the following relation was found by Young and Dupré [28],

$$\gamma_{sv} = \gamma_{lv} \cos\theta + \gamma_{sl} \qquad (1.7)$$

where θ is the contact angle (figure 1.7). For a highly wetting liquid (θ ≈ 0) the above equation reduces down to,

$$\gamma_{sv} = \gamma_{lv} + \gamma_{sl} \qquad (1.8)$$

Spreading refers to the kinetic process in which the liquid distributes itself to cover the surfaces of the particulate solid. A good spreading of the liquid is essential for enhanced densification. The total surface energy must be reduced for proper spreading to occur. So, the system always tries to reduce the interface between liquid and vapour and thereby reduce the total interface energy of the system.

For a spherical pore of radius r in a liquid, the pressure difference across the curved surface is given by the equation of Young and Laplace,

$$p = -\frac{2\gamma_{lv}}{r} \qquad (1.9)$$

The pressure in the liquid is lower than that in the pore and this generates a compressive capillary stress on the solid particles. This stress is like an external hydrostatic pressure and helps the powder-compact to shrink.

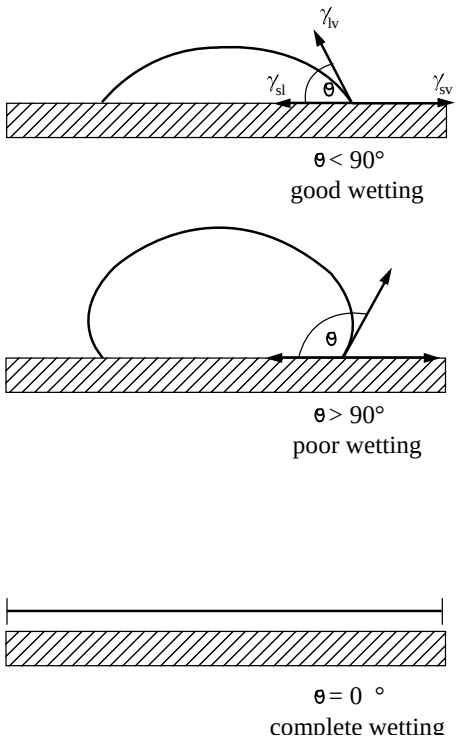

Figure 1.7: Wetting behaviour between a solid and a liquid in terms of interfacial energies showing good-, poor- and complete wetting

1.3.2 Kinetics of liquid-phase sintering

The most important densification mechanisms during liquid phase sintering are contact flattening and Ostwald ripening. Both mechanisms are active during solution and reprecipitation in the intermediate sintering stage. Figure 1.8 shows how densification is obtained through Ostwald ripening. This model, in the idealized form (as in figure 1.8), assumes that small grains dissolve and material is precipitated on the large grains away from the contact points.

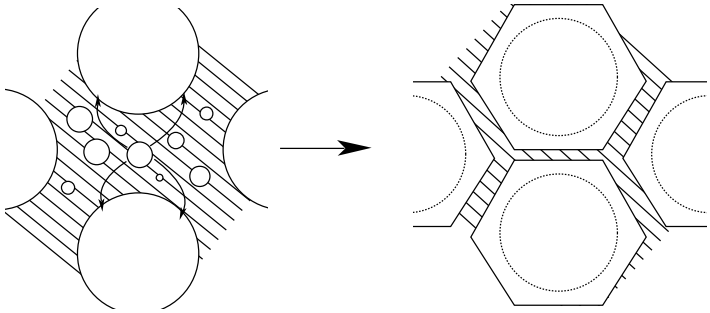

Figure 1.8: Densification accompanied by Ostwald ripening. If liquid volume fraction is low, grain-shape accommodation can also occur (redrawn from Rahaman [27])

This is accompanied by some grain-shape accommodation such that large-growing grains fill the space more efficiently giving birth to coupled polyhedron (compare figure 8) and lead to centre-to-centre approach of the large grains and thus, to shrinkage.

Both Kingery [29] and German [30] who addressed these two factors in describing liquid phase sintering, have ended up into equations of identical structure as in equation 1.10 below [29,30]:

$$-\frac{\Delta L}{L_0} = \left(\frac{C D_l \gamma_{lv}}{G^n T} \right)^{1/3} t^{1/3} \qquad (1.10)$$

$$D_l = D_0 \exp\left(-\frac{E_D}{RT}\right) \quad (1.11)$$

$$G^m = G_0^m + k_0 \exp\left(-\frac{E_G}{RT}\right) t \quad (1.12)$$

where $\Delta L/L_0$ = sintering shrinkage, C = constant depending on sintering state, D_l = diffusion coefficient of atoms of solid phase within the melt phase, γ_{lv} = energy of liquid-vapour interface, G = grain size, G_0 = initial grain size, D_0 and k_0 are constant frequency factors, R = gas constant, E_D and E_G are the activation energies for diffusion respectively grain growth, T = absolute temperature, t = time, n = scaling exponent depending on rate controlling mechanism (n=3 for Ostwald ripening and n=4 for contact flattening) and m= grain growth exponent (m=3 for diffusion controlled Ostwald ripening).

1.4 Motivation of the current work

Aim of the current project is to optimize the liquid phase sintering process by learning about the role of each component so as to influence the microstructure and obtain better varistor properties. Our results shall be combined with knowledge from other groups who have made specific suggestions on microstructural parameters that control electrical properties. This will help to grow an overall understanding of the liquid phase sintering and thereby to improve varistor systems.

1.4.1 Phase studies using Synchrotron X-Rays

Antimony changes its valence from Sb^{3+} to Sb^{5+} when spinel and pyrochlore are formed from Sb_2O_3 meaning that additional oxygen is required from the atmosphere. This can create gradients from the surface to the interior of the compacts during heat treatment when

oxygen access is limited by diffusion through the pore channels. In production furnaces oxygen access may be further limited by the large packing density of ZnO green parts. Also the burn off of binder components during binder removal can create oxygen deficient atmospheres. Antimony and bismuth oxides have a large vapour pressure which lead to some evaporation during sintering – especially at high temperatures [10, 31]. This evaporation can produce additional gradients in the components with higher concentration of volatile species in the interior of the parts. Evaporation rate depends on the partial pressure of evolved components in the furnace atmosphere which is controlled by gas flow and packing density of the parts.

Few in situ investigations were done using HT-XRD [12,32]. But in these studies Cu-K_α X-rays were used which have a penetration depth as small as 15 µm in ZnO ceramics [33]. Due to gas phase reactions discussed in the previous paragraph it was expected that the phase formation at the surface of ZBS samples can differ significantly from the phase formation in the bulk material. Therefore, in the current research work we have studied phase formation in the ZBS system in situ by HT-XRD using synchrotron X-rays. This enables the analysis of bulk samples and avoids surface effects.

1.4.2 Kinetic Field Studies

Attempts have been made to elucidate the contribution of additive oxides on the grain growth controlling mechanisms of ZnO (table 1.1). Two groups [34,35] investigated the effect of Bi_2O_3-content on the grain growth of ZnO using 1 – 4 wt% [34] and 3 – 12 wt% [35] Bi_2O_3. For the 1 – 4 wt% range the grain size of ZnO increased at initial additions but then remained constant reporting fairly consistent activation energy of 150 kJ/mol. On the other hand, for the 3 – 12 wt% range activation energy was in a range of 178 to 274 kJ/mol and

ZnO-grain growth was found to decrease with increasing Bi_2O_3 content. Spinel forming additives were studied by Senda and Bradt [36] who reported a significant reduction of ZnO grain sizes and activation energy for grain growth of 600 kJ/mol.

Two works involved ternary systems taking Al_2O_3 [37] respectively TiO_2 [38] as a third additive in the binary ZnO-Bi_2O_3 systems. Al_2O_3 and TiO_2 formed a $ZnAl_2O_4$ spinel and a Zn_2TiO_4 spinel respectively. The activation energies for grain growth were 400 kJ/mol for the alumina containing system and 360 kJ/mol for the titania containing system.

Table 1.1 Exponents and activation energies for ZnO grain growth in various ZnO based ceramic systems

Reference	Ceramic system	Grain-growth exponent, m	E_G [kJ/mol]
Senda & Bradt [34]	ZnO	3	224±16
Senda & Bradt [34]	ZnO-Bi_2O_3	5	150
[35] Dey & Bradt	ZnO-Bi_2O_3	5	178 - 274
Senda and Bradt [36]	ZnO-Sb_2O_3	6	600
Nunes [37]	ZnO-Bi_2O_3-Al_2O_3	4	400
Suzuki and Bradt [38]	ZnO-Bi_2O_3-TiO_2	3	360
Chen, Shen & Wu [39]	ZnO-Bi_2O_3-Sb_2O_3-Cr_2O_3-CoO-MnO	6	301±35

Chen, Shen and Wu [39] studied the multi-component varistor system: ZnO, Sb_2O_3, Bi_2O_3, Cr_2O_3, CoO and MnO. In this work, the grain growth kinetic exponent m was 6 and the activation energy was 301±35 kJ/mol. Table 1.1 summarizes some of the efforts to learn the kinetics of liquid-phase sintering of ZnO-based ceramics.

Five possible processes which can control the motion of the grain boundary with a spinel particle attached from position a to b (please compare figure 1.9) were summarized in this study [1] which are: (1) diffusion within the ZnO lattice, (2) the phase boundary reaction at the particle-liquid grain boundary interface, (3) diffusion through the Bi_2O_3 rich grain boundary liquid phase, (4) surface, interface or grain boundary diffusion and (5) diffusion within the spinel particle lattice itself.

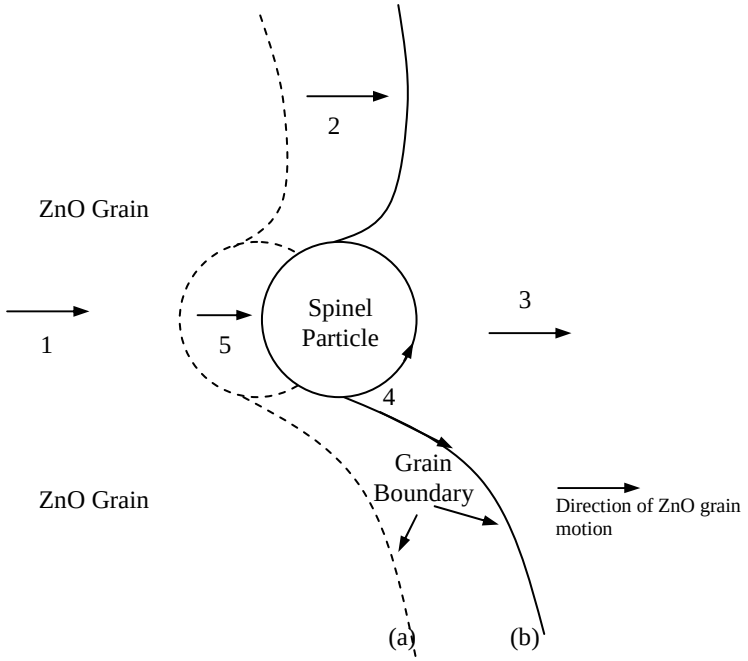

Figure1.9: schematic of a migrating ZnO grain boundary from position a to b with a spinel particle attached (redrawn from Bradt and Burkett [1])

So far no kinetic field study for the aforementioned diffusion paths have been accomplished to yield experimental activation energies related to those paths. In the current study we intended to employ a kinetic analysis of an important ternary ZnO-Bi_2O_3-Sb_2O_3 system trying to fill in the gap in knowledge about the ternary systems where both liquid phase- and spinel forming additives are present. We also tried to differentiate sample preparation techniques which can also affect particle packing and so the grain growth largely.

Chapter 2: Experimental techniques

2.1 Sample preparation

Green samples were prepared after dry milling ZnO, Sb_2O_3 and Bi_2O_3 powders (ABB, Switzerland) separately in a tungsten carbide vibrating cup mill (Fritsch Pulverisette 9, Fritsch, Idar-Oberstein, Germany) for 3 minutes each. The particle size ($D_{0.5}$) was determined in iso-propanol using laser light scattering (Mastersizer S, Malvern Instruments GmbH, Herrenberg, Germany). The particle-size data are shown in table 2.1.

Table 2.1 Mean particle size ($D_{0.5}$) of raw powders before and after milling

	ZnO (µm)	Sb_2O_3 (µm)	Bi_2O_3 (µm)
Raw $D_{0.5}$	1.82	3.29	4.42
Milled $D_{0.5}$	1.56	2.48	3.29

The milled powders were then mixed using appropriate amounts of ZnO, Bi_2O_3 and Sb_2O_3. Ratio of Sb_2O_3 to Bi_2O_3 was varied between 2:1, 1:1 and 1:2 for all the different experiments. However, the composition of the ternary mixture in HT-XRD analysis was adjusted to 94 mol% ZnO and 6 mol% additives to obtain better detection of minor phases. In contrast, for the dilatometric experiments the additive amount was fixed to 1.5 mol% with 98.5 mol% ZnO. Another batch of samples was prepared for electrical characterisation experiments by further doping the ternary (ZnO, Bi_2O_3 and Sb_2O_3) mixture with 0.5 mol% MnO. With MnO doping the total amount of the two basic additives Bi_2O_3 and Sb_2O_3 was kept at 1.5 mol% leaving the amount of ZnO at 98.0 mol%.

The isoelectric points of the powders were measured by electrokinetic sonic amplitude (ESA, AcoustoSizer II, Agilent Technologies, Inc., Santa Clara, USA) to be 8.4-9.4, 9.8 and 2.7-3.2 for ZnO, Bi_2O_3 and Sb_2O_3 respectively. Distilled water was used to prepare the slurry which had a pH value of 7.5. Mixing was done in a planetary ball mixer for 24 h. A zirconia container and zirconia balls were used to avoid any impurity from the lining. The mixture was then dried for 12 hours at 130°C and pushed through a sieve with 2 x 2 mm^2 mesh size.

The dried powders with soft agglomerates were then filled into silicon moulds and cold isostatically pressed at 100 MPa using oil based Electro-Hydraulic press (KIP 100E-KIP 500E, Paul-Otto Weber, Grunbach, Germany). Cylindrical compacts obtained after cold pressing usually have a diameter of 19 mm and green-density of 3.4 gm/cm^3 which corresponds to 60% of the theoretical density (5.606 gm/cm^3 [40]). These cylinders are directly used for in-situ optical dilatometry. For the high temperature XRD analysis they are further cut into thin discs of 1 mm thickness using SiC cutting wheel. Table 3.3 shows the dimensions of the cylindrical samples for different types of experiments.

Table 2.2 Sample dimensions (green compact)

Method	Sample diameter (mm)	Thickness (mm)	Density (gm/cm^3)
Optical dilatometry	19	20	3.39 ± 0.04
Phase analysis	19	1	3.39 ± 0.04

For electrical characterisation, cold pressed cylindrical samples were sintered in an electrically heated brick insulated sintering furnace (Nabertherm, Bremen, Germany) at a heating rate of 2 K/min up to a

temperature of 1200°C, held there for two hours and then rapidly cooled down to room temperature. For reducing the mass loss due to evaporation of melt phases samples were placed in alumina crucibles with very narrow leakage to furnace-air.

The sintered bodies were then cut and ground into small discs of roughly 12mm diameter and 1.9mm thickness. The ground samples were then prepared for electrical characterisation by evaporating Au-electrodes onto both sides of the samples using the ultra high vacuum (UHV) evaporation technique. On one side of the sample a circular Au-electrode, on the other side another smaller circular Au-electrode and a peripheral Au-ring (guard-ring) to protect against the leakage current along the sides of the sample were made (See figure 2.1).

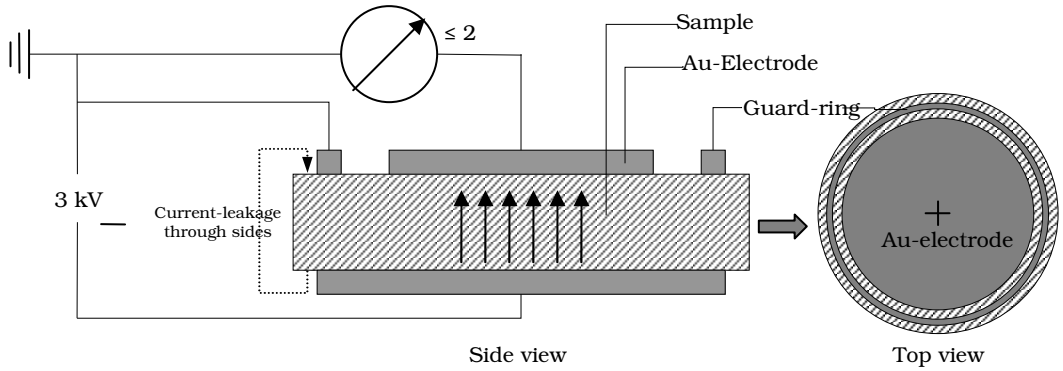

Figure 2.1: Schematic of the sample with electrodes for electrical characterisation

2.2 *In-situ* measurements

2.2.1 In-situ phase evaluation with Synchrotron X-rays

To monitor the formation of intermediate phases during sintering, high temperature X-ray diffraction was used. Since the evaporation of volatile species led to concentration gradients near the surface, HT-XRD using Cu-K_α X-rays reflects surface reactions from a depth of

merely around 15 micron [Hubell J. H., Seltzer S.M., Tables of X-Ray Mass Attenuation Coefficients and Mass Energy-Absorption Coefficients, National Institute of Standards and Technology, Gaithersburg, Maryland; /physics.nist.gov/PhysRefData/XrayMassCoef] but not the bulk properties of the varistor ceramics. Therefore, white synchrotron X-rays of high electron energy were used at the HASYLAB, Hamburg. Samples of 1 mm thickness could be analyzed in transmission.

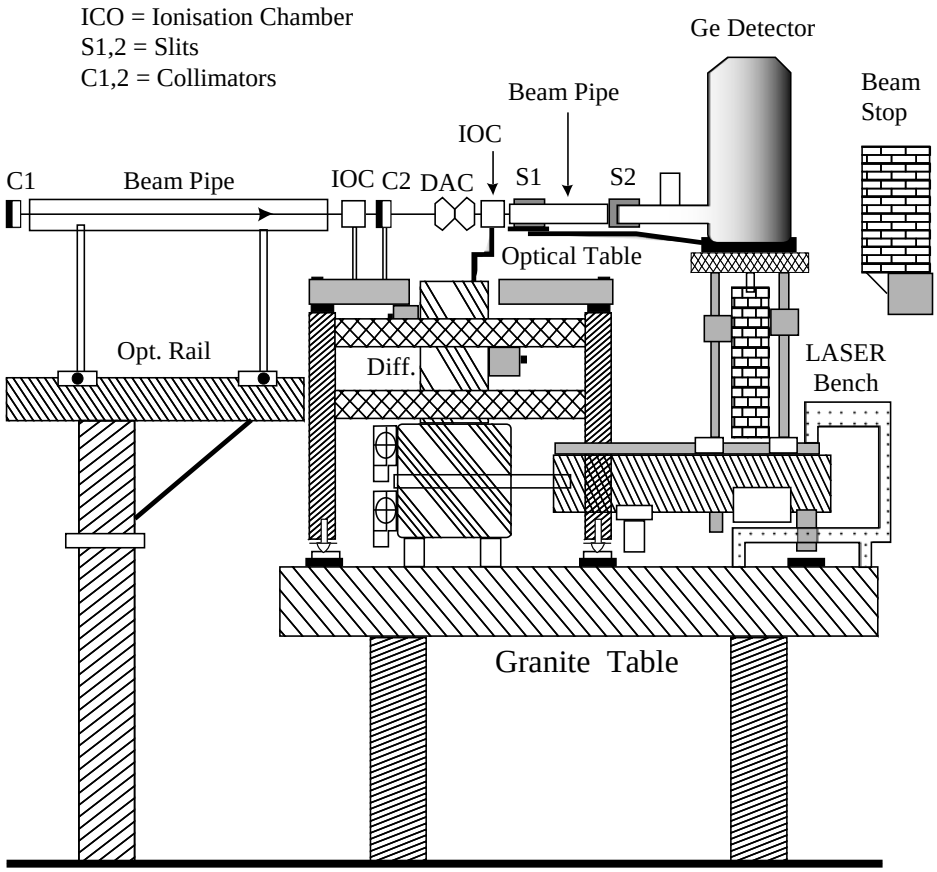

Figure 2.2: Schematic diagram of the beam station F3 (redrawn from Hasylab Web site) [56]

We have performed our in-situ high temperature X-ray measurements at the beam line F3 of the storage ring DORIS at DESY-HASYLAB. This beam station is optimized for energy dispersive diffraction measurement and specially equipped for receiving white Synchrotron

radiation from a 4.5 GeV bending magnet (Ec = 16 keV). Figure 2.2 shows the schematic drawing of the beam station. Energy resolution of the device in terms of relative change in lattice spacing ($\Delta d/d$) is $10x10^{-3}$ above 26keV. Rapid alignment is achieved by using He-Ne laser, scintillator screens, ionization chambers and a video system.

A solid-state Ge-detector with a resolution of about 1% is used for energy dispersive X-rays diffraction at an angle (2Θ) of 14.5°. Reduction of the Compton Effect is achieved using an adjustable double-slit system which rotates together with the detector and allows faster changes in angle.

Figure 2.3 shows the schematic of the experimental setup. The disc shaped samples (diameter 19 mm, thickness 1 mm) were clamped between two sintered ZnO discs with circular holes (Ø = 14 mm) in the middle to allow X-rays pass through. The entire stack goes in to the furnace which has a symmetry axis in line with the beam axis and the detector.

The main part of the furnace is built of a small resistively heated horizontal tube which is controlled through a programmable thermo-regulator. The tube, being a positive-temperature-coefficient (PTC) material, itself acted as a heating element. Unlike the traditional ones, PTC heating elements are made of doped polycrystalline ceramic based on barium titanate.

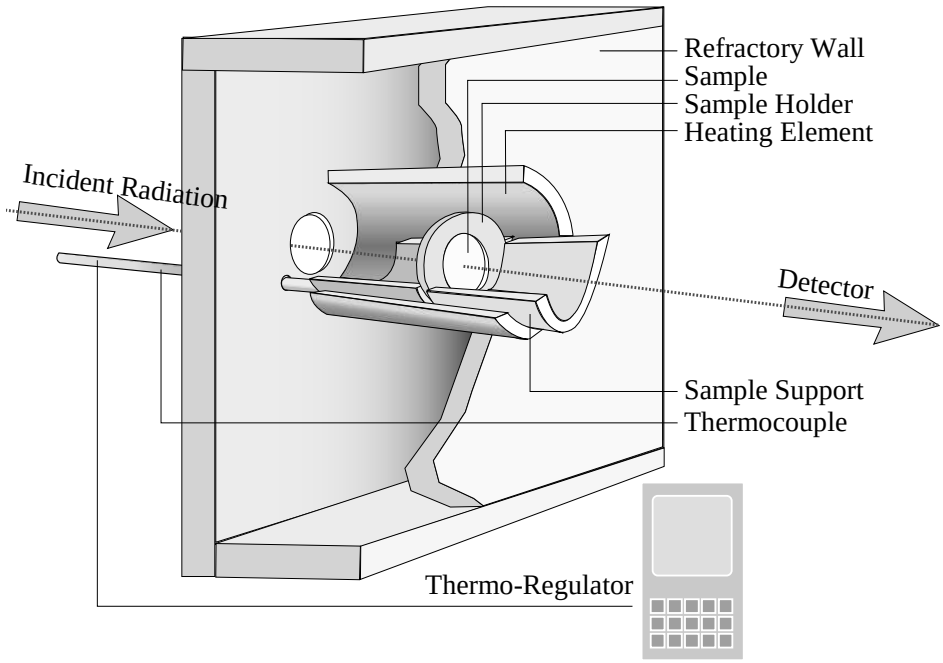

Figure 2.3: Sectioned view of the experimental setup used for HT-XRD during sintering of ZnO ceramics at the HASYLAB, Hamburg

They have unique resistance-temperature properties which causes the resistance of these materials to rise sharply at a defined temperature. Up to this temperature, which is called the switching temperature (T_s), the resistance falls consistently allowing for larger current flow and quicker heating up. But then, on reaching the switching temperature, resistance increases rapidly to heat up to temperature where it can make up for the heat loss to the ambient.

Energy calibration was done with a mixed target of Ge, Mo, Sn, Ba, W and Gd. Three different samples prepared with high additive doping (see section 2.1) were sintered at 5 K/min in ordinary air. Temperature calibration of the furnace was performed at two temperatures using the melting of Au and NaCl at 1064.18°C and 801°C respectively.

2.2.2 In-situ Optical Dilatometry

A dilatometer is an instrument to measure dimensions of solids or liquid samples which are subject to heat treatment. Materials respond to external temperature changes by an increase of their volumes which is attributed to the thermal expansion property resulting from the entropy change associated with the heat input. This property of materials is expressed in terms of thermal expansion coefficient (α) and can be measured indirectly from the relative change in dimensions as function of temperature. A dilatometer essentially consists of a heat source and a dimension-measuring sensor. The heat source is typically a furnace which can operate at high temperature (typically 1200 to 2000°C) and also which has a controllable temperature profile (heating up, holding at constant temperature for long time and cooling down etc.). The dimension measuring sensor defines the type of the dilatometer. Depending on how the expansion will be measured there are two basic types of dilatometers –

1. Push rod dilatometer and
2. Optical dilatometer

Both dilatometers are widely used for the measurements of thermal expansion or to investigate the shrinkage which occurs to porous samples during sintering. Push rod dilatometry is the conventional way of conducting such measurements where a push rod is used within the furnace. This push rod keeps direct contact to the sample and transforms the signal of sample expansion or -shrinkage to a linear variable differential transformer (LVDT) which then measures the change in the dimension occurred to the sample.

It is evident that with the incorporation of a push rod there is always some force exerted by the push rod on the sample and this will induce additional deformation to the sample when it is soft. This is specially a

problem when dealing with sintering of loose powder compacts or highly ductile materials or even polymers. Another disadvantage of push rod dilatometers could be some reaction between the push rod and the sample under observation. A non-contact method on the other hand would clearly be a better choice to get rid of this probability of unwanted interaction between push rod and the sample.

In our experiments, we have used a home-built thermo-optical measuring device called TOMMI. This method allows dimensional measurements without any physical contact to the sample under observation. With this kind of instrument it is possible to investigate materials expansion or contraction during heat treatment at a temperature between 25°C to 2000°C.

Fig. 2.4 shows the schematic drawing of the optical dilatometer. It uses the shadow of the sample to calculate its dimensional parameters. The sample is illuminated by a halogen lamp. The furnace which operates in air (flow 10 l/min) and heated by $MoSi_2$ heating elements has two round quartz windows on two opposing sides along the optical axis. These windows enable light to pass through the furnace chamber on to the other side where a C-MOS camera is installed to record the incoming light. Thus the images obtained by the camera are transferred to the computer. The sample contour is detected by a special contour tracking algorithm. Dimensional changes of the sample are extracted in-situ from the sample contour [41].

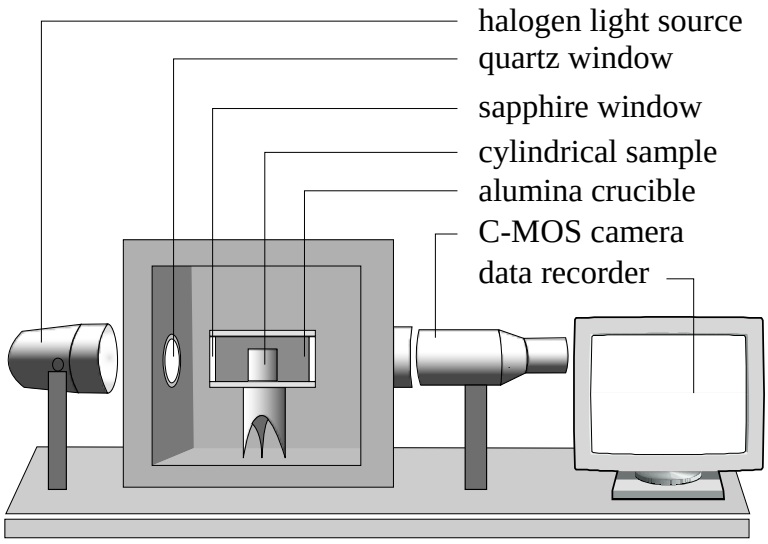

Figure 2.4: Two dimensional view of the in-situ optical dilatometer (TOMMI) made by Fraunhofer ISC in Wuerzburg, Germany

This software handles the control of the furnace and the measurement. Along with other parameters it records the temperature of the furnace. The sample usually lies on a flat substrate material during the sintering experiments. At high temperature caking of sample on the substrate material may occur. Therefore the sample is always separated by a thin layer of ZrO_2 powder from the substrate. Also, the samples were sintered in a an alumina crucible (42 x 30 x 25 mm^3) with closed lid to increase the partial pressure of gas species evolved during the heat treatment. The crucible was equipped with sapphire windows to enable light transmission (see figure 2.4).

For some special purposes the internal atmosphere was influenced by adding loose powders of Sb_2O_3 or Bi_2O_3 (app. 2 gm) in the crucible to observe the effect of atmosphere on sintering kinetics. Shrinkage L/L_0 was measured using the width of the samples scaled by the initial width at start of the measurement. Temperature was measured with a Pt-PtRh thermocouple outside the crucible. Temperature calibration was done with an additional thermocouple inside the crucible and correcting for the measured temperature difference.

2.2.3 In-situ Thermal Analyses

2.2.3.1 Differential Thermal Analysis (DTA)

Differential thermal analysis (DTA) is a technique to measure thermal responses of a material relative to a reference (inert) material while keeping both the samples under identical thermal conditions. As for the name reads, any difference in temperature between the reference and the sample under observation is recorded and plotted against temperature or time. Positive or negative changes in temperature (ΔT) are detected with reference to the inert sample and attributed to exo- or endothermic reaction taking place within the sample.

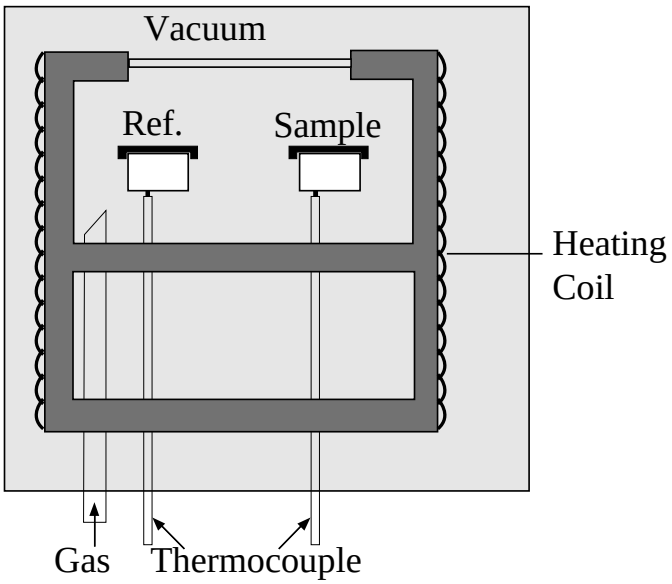

Fig. 2.5: Schematic diagram showing necessary components of a DTA device

A typical DTA apparatus (compare figure 2.5) consists of a sample holder with thermocouples, sample containers with ceramic or metallic blocks, a furnace which can be heated up by a programmable thermal regulator and a data acquisition system which can read the differences in temperature in terms of voltages.

Differential thermal analysis (DTA) was done with NETZSCH STA409 (Netzsch Gerätebau GmbH, Selb, Germany). The sample preparation was similar to that for thermogravimetric analysis and is discussed in the following section.

2.2.3.2 Thermogravimetric Analysis (TGA)

Thermogravimetry is one of the most widely used thermal analysis techniques where a samples weight change is recorded as function of temperature or time maintained in a defined atmosphere (e.g. nitrogen, helium, air, oxygen, other gas or vacuum). This method can measure mass changes in inorganic materials, metals, polymers and plastics, ceramics, glasses, and composite materials within a temperature range from 25°C to 900°C routinely. The maximum temperature is typically 1600°C. There are some limitations of maximum weight but typically sample weight can range from 1 mg to 150 mg. Sample weights of more than 25 mg are preferred, but excellent results (with a sensitivity of 0.01 mg) are sometimes obtainable on 1 mg of material. Samples can be analyzed in the form of powder or small pieces.

Samples mass change can be monitored while it's being heated, cooled or even kept at a constant temperature. Although for most reactants, sample mass usually reduces due to the evaporation of absorbed or chemically bond water, decomposition or evaporation of materials, there are samples for which weight increase is also observed. This occurs when samples experience oxidation or carbonatisation within the defined atmosphere of the crucible.

This kind of thermal analyses typically include a high sensitivity balance, a temperature-controlled furnace, a unit for evacuation and control of the atmosphere in the furnace, and units for control and

data recording. Thermogravimetry (TG) was conducted using a thermobalance (SETARAM TAG24, Setaram, Caluire Cedex, France).

Binary mixtures of the raw powder were prepared with ZnO and Sb_2O_3 and with ZnO and Bi_2O_3 at a molar ratio of 1:1. Small disc shaped samples with 10 mm diameter and 2 mm thickness were formed from these mixtures and heated at 10 K/min up to 1000°C in atmospheres of O_2-, Ar- and synthetic air, respectively.

2.2.4 Optical measurement of wetting properties

Wetting of ZnO by the melt phase was investigated by the sessile droplet method using the thermooptical measuring device already described with the optical dilatometry. For comparison a binary (90 vol% Bi_2O_3 and 10 vol% ZnO) and a ternary mixture (90 vol% Bi_2O_3, 5 vol% ZnO and 5 vol% Sb_2O_3) were prepared. The binary- and ternary-mixtures were heated individually in an alumina crucible to 740°C and 815°C respectively. Then the crucible was rotated to cast the melt on to the flat ZnO sample where it formed a droplet. The contact angle was determined by fitting an ellipse to the droplet contour and by measuring the angle between the horizontal contour line of the ZnO sample and the tangents to the ellipse at the intersection with the horizontal line.

2.3 Sample Characterisation

A variety of sample characterisation techniques were used at ambient temperature in this study e.g. secondary electron microscopy (SEM) and EDX for compositional studies, XRD for phase evaluation and J-V characterisation for current-voltage characteristics.

2.3.1 Scanning electron microscopy (SEM)

Scanning electron microscopy was used to analyze quenched ZnO-Bi_2O_3-Sb_2O_3 (ZBS) samples. Quenching of the ZBS samples was done after heating them in the same horizontal tube-furnace which was used for HT-XRD phase evaluation (see figure 2.3). Samples with 2 mm thickness and 10 mm diameter were heated with a heating rate of 10 K/min to 800-, 900-, 1000- and 1100 °C and then rapidly quenched using a liquid nitrogen bath. Quenched samples were then fractured along the flat surface and polished in successive runs using SiC (25- and 15 μm), diamond (3 μm) and finally CeO (1 μm). Polished samples were investigated in scanning electron microscope (SEM) with backscattered electrons (SUPRA, Carl Zeiss AG, Oberkochen, Germany). The microstructure was analysed by lineal intercept methods using Image-C software (IMTRONIC GmbH, Berlin, Germany).

2.3.2 Room Temperature X-Ray analysis

Room temperature XRD analysis was done to identify the basic metal-oxide powders which were used in our experiments. There were two different Bragg-Brentano diffractometers used for phase evaluations – Phillips (mBraun GmbH, Garching, Germany) with position sensitive detector and Siemens D-5005 (Axs GmbH, Karlsruhe, Germany) in Fraunhofer, Germany and ABB, Switzerland respectively. Diffractograms of the Cu-Kα were obtained between 10 and 60 degrees for both green and sintered samples.

2.3.3 Electrical Characterisation

Electrical characterisation of the doped and non-doped samples (see paragraph 2.1) were done in the research facility of ABB, Switzerland during a scientific stay using their home built software *DC3 Collect*

Data 11. Samples were set up for characterisation in the way as shown in figure 2.1.

Two batches of samples were analysed for their electrical properties (J-V) – one batch was ZBS samples doped with MnO. These samples were sintered at 2 K/min and checked for their J–V properties against their Sb:Bi ratio and thus electrical properties were compared for different samples with different Sb:Bi ratios of 1:1, 1:2 and 2:1. The second batch of samples was not doped with MnO and was checked for their electrical properties (J-V) against the heating rate of sintering and thus J-V characteristics were measured for different heating rates of 1-, 2-, 5- and 10 K/min.

Chapter 3: Data Evaluation

3.1 Room- and high Temperature XRD evaluation

Any kind of X-rays diffraction analysis is based on the solution of Bragg's equation for diffraction which is as following,

$$2d \sin\theta = n\lambda \qquad (3.1)$$

d being the distance of two parallel lattice planes, θ –the angle of diffraction (also called Bragg angle) and λ -the wave length of the diffracted radiation.

In case of energy dispersive X-ray diffraction opposed to standard angle dispersive analysis, we keep the Bragg angle constant by keeping the detector at a fixed angle where it receives the maxima of the diffracted beam during the experiment. This is possible since the value of the lattice plane distance is determined experimentally from the value of the wave length (λ) of the diffracted beam of the original polychromatic radiation [42]. The difference of the two methods can be understood better from figure 3.1.

In this type of measurement the energy scale, instead of the angle of incidence, is varied throughout the scan and diffracted radiation is detected from a fixed angle.

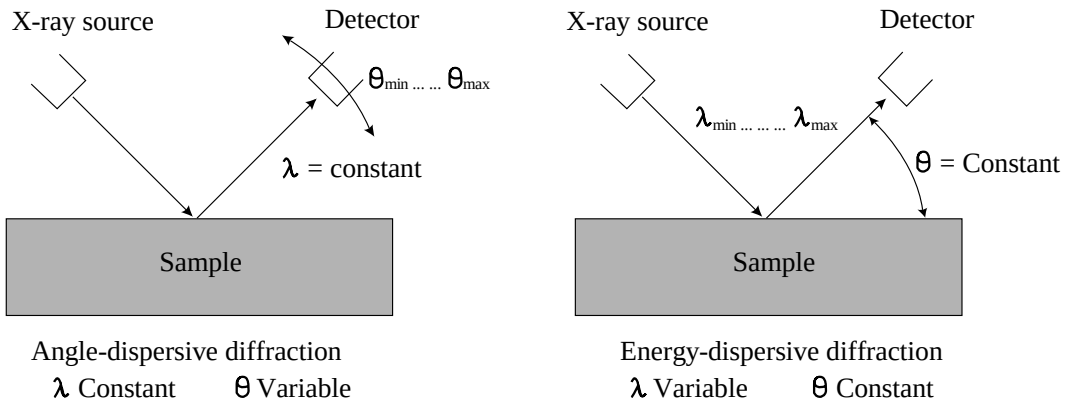

Figure 3.1: Comparison of angle- and energy dispersive X-ray diffraction (redrawn from Kämpfe et al [42])

For each diffraction peak the interplanar spacing *d* can be obtained from Bragg's equation if written in terms of photon energy *E* associated with that particular peak,

$$Ed\sin\theta_0 = \frac{hc}{2} = 6.199 keV\,\text{Å} \qquad (3.2)$$

where, θ_o is the fixed Bragg angle, *h* Plank's constant and *c* is the velocity of light. The peak positions have been determined by converting the data into conventional 2θ –scale and then comparing with standard peak positions.

The phase evaluations were done after converting the in-situ data from energy scale (channels) to angular scale (2θ) according to the wavelength of Cu-K_α X-rays (0.154 nm) using the DIFFRAC*plus* evaluation package (Bruker AXS GmbH, Karlsruhe, Germany). The database used for phase identification was ICSD (Fachinformationszentrum FIZ, Karlsruhe, Germany). Peak areas of important peaks were determined after subtraction of a linear background. The respective peak areas were scaled by the area of the <102> ZnO peak in the corresponding spectrum.

Some efforts were made to perform Rietvelt refinement on our in-situ XRD data to clarify the minor peaks but due to the unavailability of high temperature crystalline phase-data, the refinement could not be done. Nevertheless, the quality of the data evaluation was adequate for our purposes and successful interpretation of the phase evaluations during liquid-phase sintering was possible.
Room temperature X-ray data were evaluated and peak matching was done using the same DIFFRAC*plus* evaluation package as above.

3.2 Thermodynamic Simulation

The aim of thermodynamic modelling was to address melt formation, its compositional range, stability of solid phases and the effect of oxygen fugacity on the progress of sintering. We have compiled a thermodynamic dataset for solid, liquid and gaseous species in the system Bi-Sb-Zn-O [31]. The liquid phase in the Bi-O system is described by the two-sublattice ionic model [43] whereas the multicomponent oxide liquid is best reproduced by an associate model with small symmetric contribution to the enthalpy of mixing (-13 kJ/mol) between ZnO and Bi_2O_3, and ZnO and Sb_2O_3. The gas phase was considered an ideal mixture of multiple oxide species.

Two different packages were simultaneously used for the thermodynamic simulations – Factsage [31] and Theriak-Domino code [44]. Factsage is a commercial software developed by the collaboration between CRCT (Montreal, Canada) and GTT-Technologies (Aachen, Germany) while the other package is an open source developed by Christian de Capitani (Mineralogisch-Petrographisches Institut, Universität Basel, Switzerland).

3.3 Image post-processing and statistical analysis

Image post-processing was done by the lineal intercept method using Image-C software (see section 2.3.1) to obtain statistical data on microstructural parameters e.g. grain-size, pore-size, their distributions, standard deviation etc. The lineal intercept method was realised by drawing lines across SEM-images showing three specific grey-scale values corresponding to ZnO, intra-grain phase and pores. Next, the intercepts along these lines with the phase boundaries were distinguished and marked. The software then automatically performed basic statistical operations on the numbers of the intercepts and chord-lengths. While interpreting the statistical data obtained from such evaluation technique one has to consider that, chord-length is an indirect way of describing the distributions of microstructural quantities and may only be expressed as grain-size or fractions after performing conversion using a proper conversion-factor obtained from appropriate models. The chord lengths of ZnO grains followed a log-normal distribution, so, we have used Mendelsons model [45] to obtain grain-size values from calculated chord lengths according to the following relation,

$$G = K_M L_c \tag{3.3}$$

where, G is average grain size in 3-D, K_M is Mendelsons conversion constant and L_C is the average chord-length. The value of K_M was chosen to be 1.56 according to Senda *et al* [34].

Standard error of the mean was calculated according to the following formula,

$$SE = \frac{\sigma}{\sqrt{N}} \tag{3.4}$$

where, SE is standard error of the mean, σ is standard deviation and N is the total number of chord-lengths.

3.4 Evaluation of the dilatometric data

3.4.1 Correction for thermal expansion

Prior to evaluation of the shrinkage data obtained from TOMMI correction for thermal expansion was done by a 2nd order polynomial fitted to the expansion-curve obtained from a pre-sintered body in the required temperature range. Onset temperature of sintering was determined from the $L/L_0(T)$ curve by the intersection of the tangents before shrinkage and at 1 % shrinkage.

3.4.2 Kinetic data evaluation

As described in section 1.3.2, equation 1.10 describes our liquid phase sintering system. Strain rates were calculated by time derivation of the experimental shrinkage curves:

$$\dot{\varepsilon} = \frac{dL}{L\,dt} \tag{3.5}$$

where ε = true strain, L = diameter of the sample.

To investigate the interaction of grain growth and densification in more detail equation 1.10 and 3.5 were transformed to use it in the kinetic field diagram. Time derivation, substitution of t and rearrangement leads to:

$$\ln\left(-\delta T \dot{\varepsilon}\right) = \ln\left(\frac{C' D_l \gamma_{lv}}{G^n}\right) = \ln\left(\frac{C' D_0 \gamma_{lv}}{G^n}\right) - \frac{E_D}{RT}; \tag{3.6}$$

$$\delta = \frac{\Delta L^2 L}{L_0^3}$$

with C' = constant depending on density (different from constant C in equation 1).

By plotting the left hand side of equation 3.6 versus inverse absolute temperature 1/T liquid phase sintering kinetics can be directly compared to the models. Points representing equal strain on the different strain rate curves were connected to form the so-called iso-strain lines. Details of the method were described by Palmour [48]. It can be seen that the iso-strain lines form straight lines. Due to the Arhenius type diagram used, the slope of these lines can be interpreted as apparent activation energy for densification (Figure 4.14). Since different mechanisms interact during densification, the apparent activation energy doesn't correspond to one specific mechanism [41].

Chapter 4: Results

4.1 Phase formation during liquid phase sintering of ZnO ceramics

4.1.1 Thermodynamic simulations

Fig. 4.1 shows that partial pressure of oxygen, i.e. oxygen fugacity has a significant effect on the stability of antimony oxides.

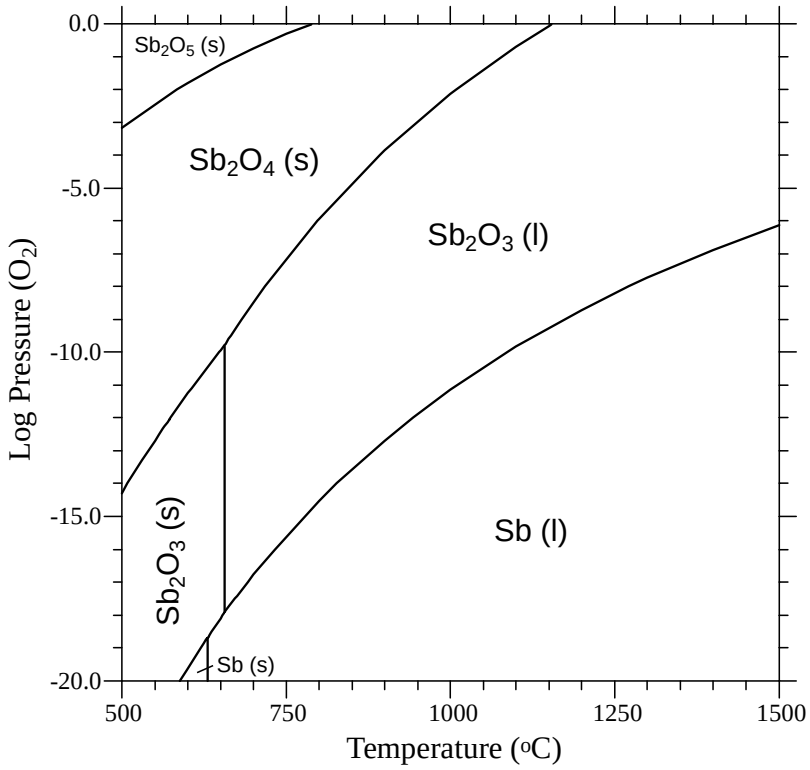

Figure 4.1: Equilibrium states in the Sb-O system as a function of temperature and O_2 partial pressure [49]

At low temperatures in air, Sb_2O_5 is stable but it becomes progressively reduced to Sb_2O_4 at 780 and to Sb_2O_3 at 1150°C. Sb_2O_4 is predicted to be a stable phase within the range of our experimental temperature and pressure (750 - 1150°C, 0.2 - 1 bar), see also [24]. It

is, therefore, possible that solid Sb_2O_4 forms during initial stages of sintering and it restricts melt productivity due to its refractory character. This is in agreement with our HT-XRD results.

In the Bi-O system, the Bi_2O_3 phase is stable over the whole temperature range (Fig. 4.2). α-Bi_2O_3 undergoes solid-solid transformation to the δ-polymorph at 730°C and the latter melts at 825°C. At high temperatures increasing miscibility between Bi_2O_3 (l) and Bi(l) is responsible for variation of melt composition with oxygen partial pressure. At oxygen saturation, the calculated liquid composition remains very close to Bi_2O_3.

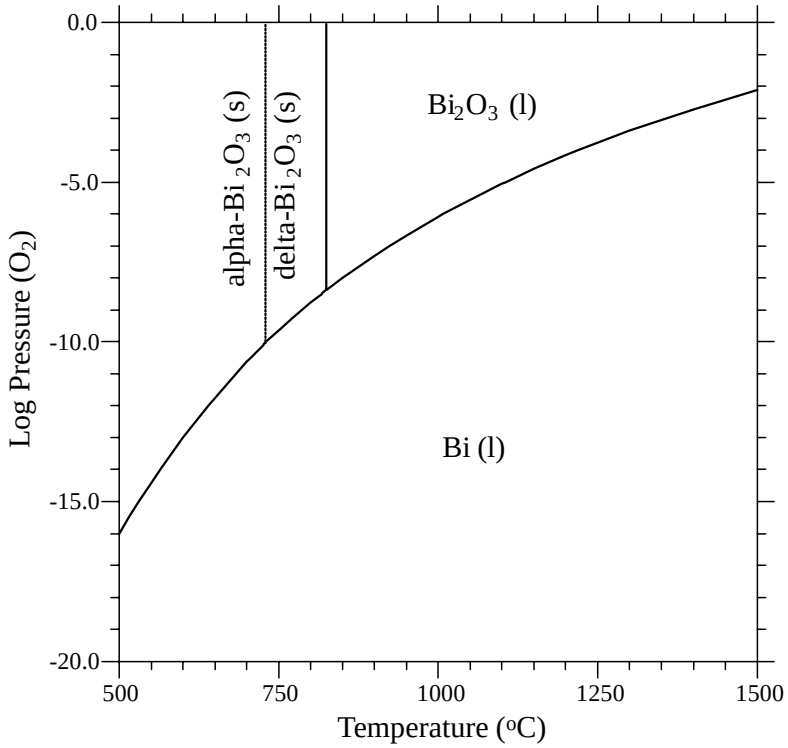

Figure 4.2: Equilibrium states in the Bi-O system as a function of temperature and O_2 partial pressure [49]

During sintering, starting oxides (Bi_2O_3, Sb_2O_3) undergo vaporization which creates undesirable gradients in the composition and porosity near the sample surface. In order to assess the gas composition and

factors that can control it gas speciation and vapour pressures of individual species were calculated (Fig. 4.3).

In the system Sb-O, the vapour is dominated by Sb_4O_6 species with a vapour pressure of $10^{-1.8}$ bar at 1000°C (Fig. 4.3a). Elemental gaseous species (Sb, Sb_2 and Sb_4) have partial pressures less than 10^{-12} bar over the molten oxide and are not significant for selective element removal. In the system Bi-O, vapour pressures vary over several orders of magnitude and reach 10^{-4} bar at 1000°C in air or oxygen (Fig. 4.3b). The predominant gaseous species is Bi_4O_6, followed by Bi_2O_3.

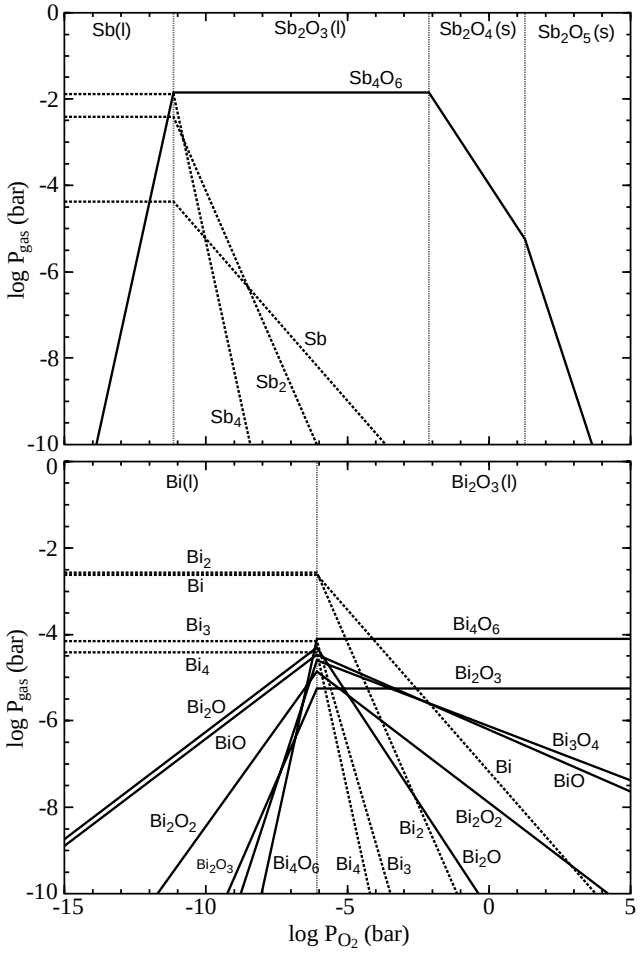

Figure 4.3: Vapour pressure over (a) Sb_2O_3- and (b) Bi_2O_3 liquid shown as a function of O_2 partial pressure at 1000°C [49]

Vapour pressure of BiO and Bi_3O_4 are two orders of magnitude lower. The results demonstrate that Bi_2O_3 vaporizes congruently but less efficiently than Sb_2O_3. Reduced gaseous species of bismuth become only stable at extremely reducing conditions where the vapour pressures increase significantly.

Melt formation during sintering was modelled in the Zn-Bi-O and Zn-Bi-Sb-O systems. Fig. 4.4 shows pseudo-binary temperature-composition sections. The system Bi_2O_3-ZnO is characterized by a strongly asymmetric location of the binary eutectic at 750°C and 89 mol % Bi_2O_3. The initial melt dissolves minor quantities of zinc oxide only; therefore the amount of melt in the system is controlled by the initial Bi_2O_3 proportion in the sample. Addition of Sb_2O_3 to the system leads to depression of the solidus from 750 to 590°C (Figure 4.4b) due to the comparably low melting temperature of Sb_2O_3. As in the previous case, the low-temperature melt is dominated by $(Bi,Sb)_2O_3$ and it contains less than 10 mol % dissolved ZnO.

Fig. 4.4c shows the melt formation in the Bi_2O_3-Sb_2O_4-ZnO ternary which corresponds to more oxidizing conditions than the system with Sb_2O_3. Sb_2O_4 is a refractory oxide and the onset of melting changes accordingly. The system is pseudoternary and the eutectic melting is not depressed to below 760°C. At these conditions, four phases are present: $(Bi,Sb)_2O_3$ liquid and Sb_2O_4, Sb_2O_5 and ZnO solid phases. At 790°C, Sb_2O_5 disappears and the liquid is saturated with ZnO and Sb_2O_4.

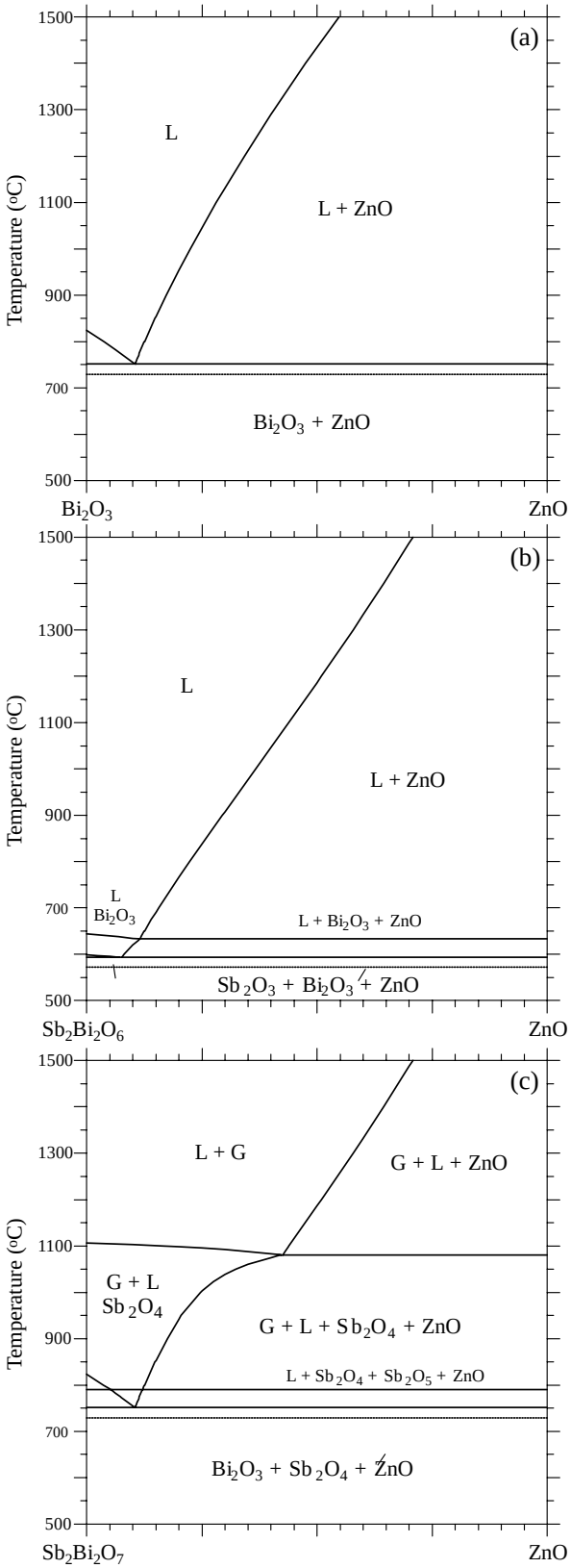

Figure 4.4: Calculated temperature-composition sections for (a) ZnO-Bi_2O_3, (b) ZnO-Bi_2O_3-Sb_2O_3 and (c) ZnO- Bi_2O_3-Sb_2O_4 (L = liquid, G = gas) [49]

4.1.2 Thermal analysis

The binary system ZnO-Sb_2O_3 (molar ratio 1:1) showed a weight gain of 4.6% during heating in pure oxygen atmosphere between 510 and 550°C (Figure 4.5). This weight gain was attributed to the oxidation from Sb_2O_3 to Sb_2O_4 which should result in an increase of 4.3%. In air a similar weight gain of 3.5% was measured between 520 and 600°C. In argon atmosphere a distinct mass loss of 76% was registered between 520°C and 920°C. This mass loss corresponds to a complete evaporation of antimony oxide. The bend in the curve (compare Figure 4.5) indicates that reduction of antimony precedes evaporation.

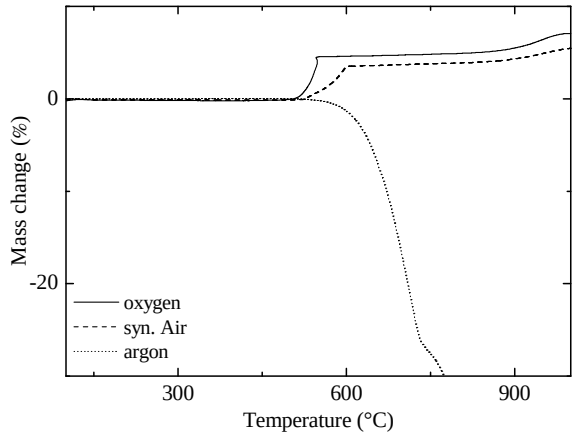

Fig. 4.5: Mass change as function of temperature of ZnO-Sb_2O_3 sample while heated at 10K/min up to 1000°C

The binary sample ZnO-Bi_2O_3 (1:1 molar) showed a weight loss of less than 0.5% regardless of the atmosphere.

Figure 4.6 shows DTA curves for the binary system ZnO-Bi_2O_3 (molar ratio 1:1) from three different experiments performed with different atmospheres. An endothermic peak at 749°C was observed for inert and oxidising atmosphere. It was attributed to the eutectic melting of the ZnO-Bi_2O_3 system.

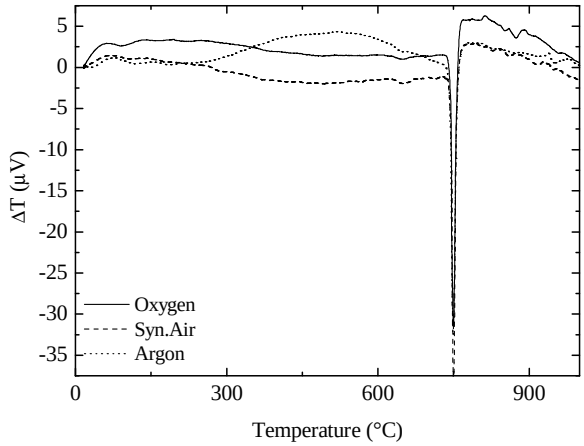

Figure 4.6: DTA curves of ZnO-Bi_2O_3 sample showing coincidence of the eutectic point at 749°C regardless of atmosphere.

4.1.3 Optical dilatometry

Figure 4.7 shows the shrinkage curves of two ZBS samples with 1.5 mol% additives (0.75 mol% Bi_2O_3 and 0.75 mol% Sb_2O_3) sintered in a closed and an open crucible respectively. Onset temperature was slightly smaller and density was significantly reduced in the open crucible (table 4.1).

Table 4.1 Onset temperatures of shrinkage, densities at 1080°C and final densities of ZBS samples sintered in a closed and open crucible respectively

Samples	Onset temp. [°C]	Density at 1080°C (from Shrinkage data) [% of theoretical density]	Final density (by Archimedes) [% of theoretical density]
Open	792	93.67	97.86
Closed	798	95.33	98.20

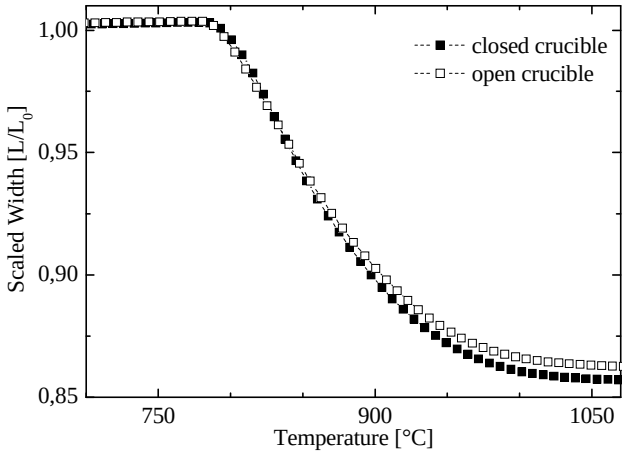

Figure 4.7: Shrinkage of ZnO green samples with ratio of Sb_2O_3 to Bi_2O_3 of 1:1 measured with (■) and without (□) a closed crucible

Figure 4.8 shows shrinkage curves for ZBS green samples with 6 mol% additives (3 mol% Bi_2O_3 and 3 mol% Sb_2O_3) sintered in different atmospheres. For the ZBS sample without additional loose powders shrinkage started at 780°C. With the addition of loose Sb_2O_3 powder within the alumina crucible, the onset temperature decreased to 762°C. This was attributed to the oxidation of Sb_2O_3 to Sb_2O_4 which created a reducing atmosphere within the crucible.

It was assumed that the reducing atmosphere led to a lower oxidation state of antimony within the sample and – according to the thermodynamic simulation - to a smaller temperature of melt formation (compare previous section). At higher temperatures the addition of Sb_2O_3 powder reduced sintering activity (compare Figure 4.8) which could not be explained yet. The final sintering stage could not be measured with the addition of loose powders since increasing condensation of volatile species at the sapphire windows of the crucible led to opaque layers at temperatures above 900°C. With the addition of loose Bi_2O_3 powder the onset temperature only slightly changed to 790°C. The decrease of onset temperature from 798°C to 780°C when ZBS samples with 1.5 respectively 6 mol% additives

where sintered in a closed crucible without loose powder was attributed to the increasing fraction of melt phase.

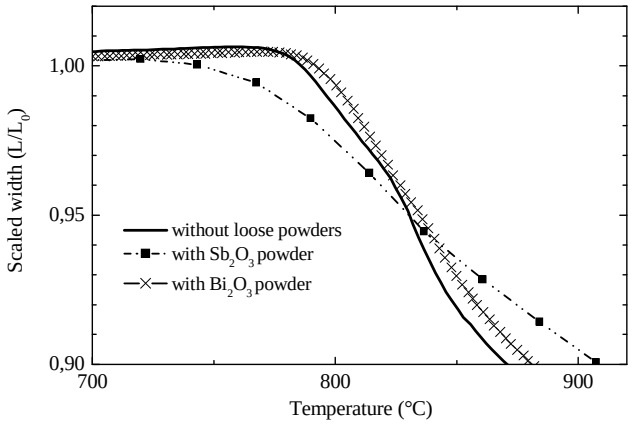

Figure 4.8: Effect of Sb_2O_3- and Bi_2O_3 powders addition in closed crucible on the onset of shrinkage in ZBS green samples

4.1.4 High temperature X-ray diffraction

Figure 4.9 shows the HT-XRD spectra of the ZBS system at a ratio of Sb_2O_3 to Bi_2O_3 of 1:1. Heating rate was 5 K/min. Besides ZnO, different polymorphs of Bi_2O_3 and Sb_2O_3, trirutile, pyrochlore and spinel were identified. From each phase one prominent peak was selected for area determination: <041> for Bi_2O_3, <440> for Sb_2O_3, <134> for γ-Bi_2O_3, <113> for β- Sb_2O_4, <433> for $Bi_{38}ZnO_{60}$, <440> for pyrochlore, <511> for spinel, <482> for beta-spinel and <213> for tri-rutile. Peak area was determined after subtraction of a linear background. The respective peak areas were scaled by the area of the <102> ZnO peak in the corresponding spectrum. Scaled peak areas are shown in Figure 10 for the 1:1, 1:2 and 2:1 ratios of Sb_2O_3 to Bi_2O_3. It can be seen that the molar ratio of the additives largely affected phase formation. In all measurements, the primary additives disappeared below 630 °C. Between 500 and 800°C γ- Bi_2O_3 and between 440 and 580°C β-Sb_2O_4 were formed. Note that the temperature of Sb_2O_4 formation is smaller than in the DTA-TG

measurement which was attributed to inaccurate temperature measurement in the tube furnace used for the HT-XRD measurements in the low temperature regime.

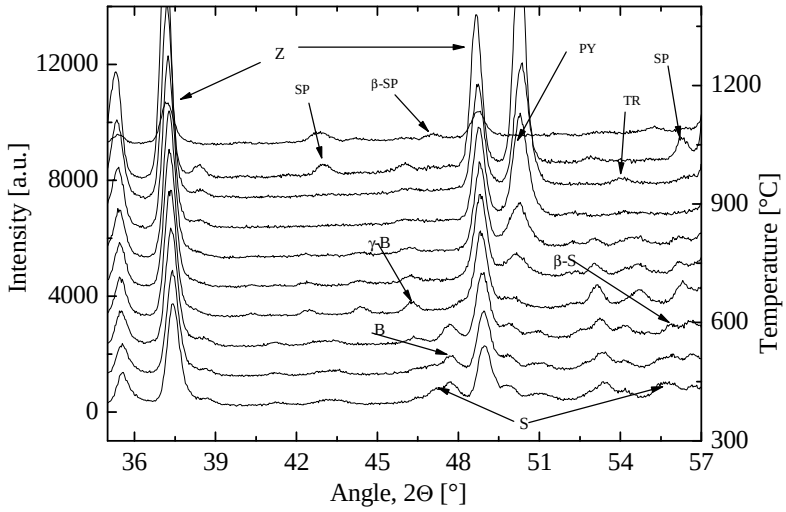

Figure 4.9: HT-XRD spectrum showing evolution of phases as functions of temperature. ZnO (Z), Bi_2O_3 (B), γ-Bi_2O_3 (γ-B), Sb_2O_3 (S), β- Sb_2O_4 (β-S), $Bi_{38}ZnO_{60}$ (BZ) and pyrochlore (PY)

Tri-rutile was formed between 750 and 1000°C in samples with molar ratios of Sb_2O_3 to Bi_2O_3 of 1:1 and 2:1 but not with 1:2. On the other hand, a binary phase $Bi_{38}ZnO_{60}$ was detected between 650 and 860°C only for the sample with 1:2 ratio (compare Figures 4.10- a, b and c). Moreover, no Spinel phase was identified for sample with molar ratios of Sb_2O_3 to Bi_2O_3 of 1:2 up to 1100°C. This was in agreement with findings of Inada [11] for a sample with similar ratio between the two additives.

The pyrochlore phase appeared little above 600°C and was stable until very high temperature beyond 1000 °C. It showed an increase up to temperatures of 1040°C and a decrease above that temperature. The increase was less pronounced with higher Sb_2O_3 to Bi_2O_3 ratio (compare Figure 4.9). With the 1:1 and 2:1 molar ratios, a spinel

phase occurred above 850°C and remained until the end of the process. It was accompanied by a polymorph (β-spinel) at high temperature. The spinel phase showed an increase at 1040°C when the pyrochlore phase decreased. Trirutile and the spinel phases were detected at lower temperatures in the sample with Sb_2O_3:Bi_2O_3 ratio of 2:1 than in the sample with 1:1 ratio. All the various phases evolved during the sintering of ZBS samples with different Sb_2O_3:Bi_2O_3 ratios are collected in table 4.2 for comparison.

Table 4.2 phase evolution for samples with various Sb/Bi-ratio.

Sb/Bi	Up to 400°C	400 – 600°C	600 – 800°C	800 – 1000°C
1:2	Bi_2O_3, Sb_2O_3, ZnO	Bi_2O_3, Sb_2O_3, ZnO, γ-Bi_2O_3, β-Sb_2O_4	ZnO, γ-Bi_2O_3, $Zn_2Bi_3Sb_3O_{14}$, $Bi_{38}ZnO_{60}$	ZnO, $Zn_2Bi_3Sb_3O_{14}$, $Bi_{38}ZnO_{60}$
1:1	Bi_2O_3, Sb_2O_3, ZnO	Bi_2O_3, Sb_2O_3, ZnO, β- Sb_2O_4	ZnO, γ-Bi_2O_3, $Zn_2Bi_3Sb_3O_{14}$	ZnO, $Zn_2Bi_3Sb_3O_{14}$, $ZnSb_2O_6$, $Zn_7Sb_2O_{12}$, β-$Zn_7Sb_2O_{12}$,
2:1	Bi_2O_3, Sb_2O_3, ZnO	Bi_2O_3, Sb_2O_3, ZnO, β- Sb_2O_4	ZnO, γ-Bi_2O_3, $Zn_2Bi_3Sb_3O_{14}$, $ZnSb_2O_6$	ZnO, $Zn_2Bi_3Sb_3O_{14}$, $ZnSb_2O_6$, $Zn_7Sb_2O_{12}$, β-$Zn_7Sb_2O_{12}$,

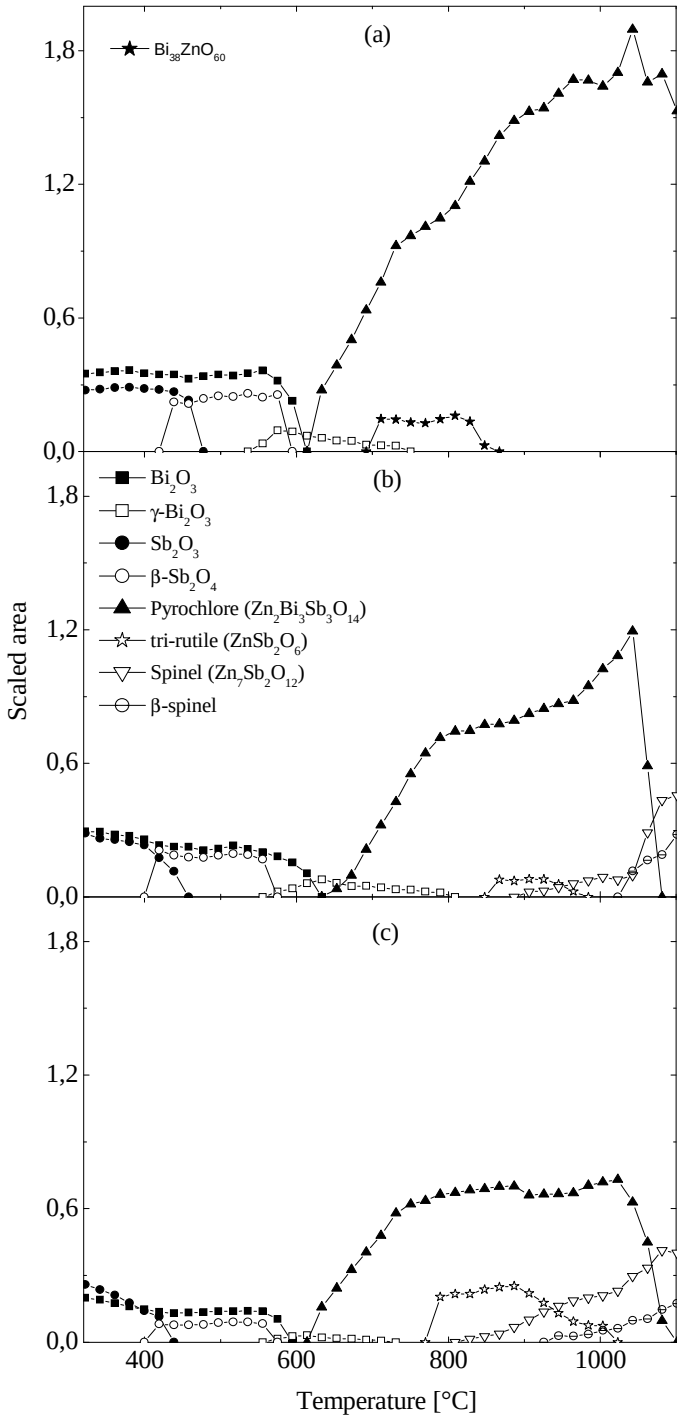

Figure 4.10: Scaled peak areas of phases identified during sintering of ZBS samples with the ratio of Sb_2O_3 to Bi_2O_3 of 1:2 (a), 1:1 (b) and 2:1 (c)

4.1.5 Discussion

The present HT-XRD and TG measurements show, that the reaction sequence during heating of ZBS samples suggested by Leite (compare equation 1.3 to 1.6 in section 1.2.1) has to be changed. In oxidizing atmospheres Sb_2O_4 is formed from the sequioxide at 530°C instead of Sb_2O_5. The formation of Sb_2O_4 during the ZBS heat treatment was already reported by Inada [5,11]. Thermodynamic modelling demonstrated that the presence of Sb_2O_4 increases the temperature of melt formation whereas Sb_2O_3 leads to a decrease of melting temperature. So it was assumed that the oxygen activity in the furnace atmosphere affects the onset temperature of sintering. This was demonstrated in sintering experiments in closed crucibles where the reducing atmosphere was generated by excess Sb_2O_3 powder. A clear decrease of the onset temperature confirmed the thermodynamic model.

Kim et al. have explained the densification characteristics of ZnO doped with Sb_2O_3 by the specific evaporation-condensation behaviour of Sb_2O_3 [13]. Antimony oxides begin to evaporate at approx. 500°C. They condense on the ZnO particle surfaces as a non-crystalline phase and moderate mass transfer and densification. This mechanism has been confirmed by several independent experimental studies [46, 47]. If Sb_2O_3 was oxidized to Sb_2O_4 the vapour pressure is strongly decreased (compare figure 4.3a) and evaporation-condensation is assumed to be retarded. So, beside melt formation, a second phenomenon exists which is affected by the oxygen activity in the atmosphere. Although not directly measured, it was concluded from the change in sintering kinetics in the intermediate stage (compare Fig. 4.8) that oxygen activity also affects the formation of phases where Sb is in the oxidation state +5 (pyrochlore, spinel).

It was argued that Bi which is bound in the pyrochlore phase is not available for melt phase formation [18]. Therefore liquid phase sintering is reduced. Kim *et al* had already shown that shrinkage was more affected by the ratio of Sb_2O_3 to Bi_2O_3 than by the absolute concentration of the additives [18]. So, the increase of pyrochlore intensity identified in the HT-XRD measurements at temperatures between 600°C and 1050°C is assumed to reduce the melt phase. The decrease of pyrochlore phase measured at higher temperature and the corresponding increase of spinel intensity is believed to increase the melt fraction. This was already proposed by Kim [18].

The thermodynamic analysis in the current work suggests that the trivalent metal oxides Bi and Sb vaporize congruently. By increasing their partial pressure in the environmental atmosphere the vaporization from the sample can be reduced during sintering. Experiments showed that sintering inside closed crucible considerably improves final densities of ZnO ceramic system compared to open sintering.

4.2 Kinetic field approach to study liquid phase sintering of ZnO based ceramics

4.2.1 Optical dilatometry

Figure 4.11a shows shrinkage curves of ZBS green samples where the molar ratio of Sb_2O_3 to Bi_2O_3 was varied whereas the total concentration of additive materials was kept at 1.5 mol%. It can be seen that the onset of shrinkage decreased from 970 °C, to 944°C and 790 °C when the Sb_2O_3 to Bi_2O_3 ratio was decreased from 2:1, to 1:1 and 1:2. Note that these samples were prepared from dry mixed unmilled powders.

Figure 4.11b shows shrinkage curves for ZBS green samples which were prepared from wet milled powders with a constant molar ratio of Sb_2O_3 to Bi_2O_3 of 1:2 sintered at different heating rates between 1- and 10 K/min. Onset of shrinkage increases from 757°C to 796°C with increasing heating rate. The onset at 5 K/min is 780°C which corresponds to 790°C for the dry mixed powder.

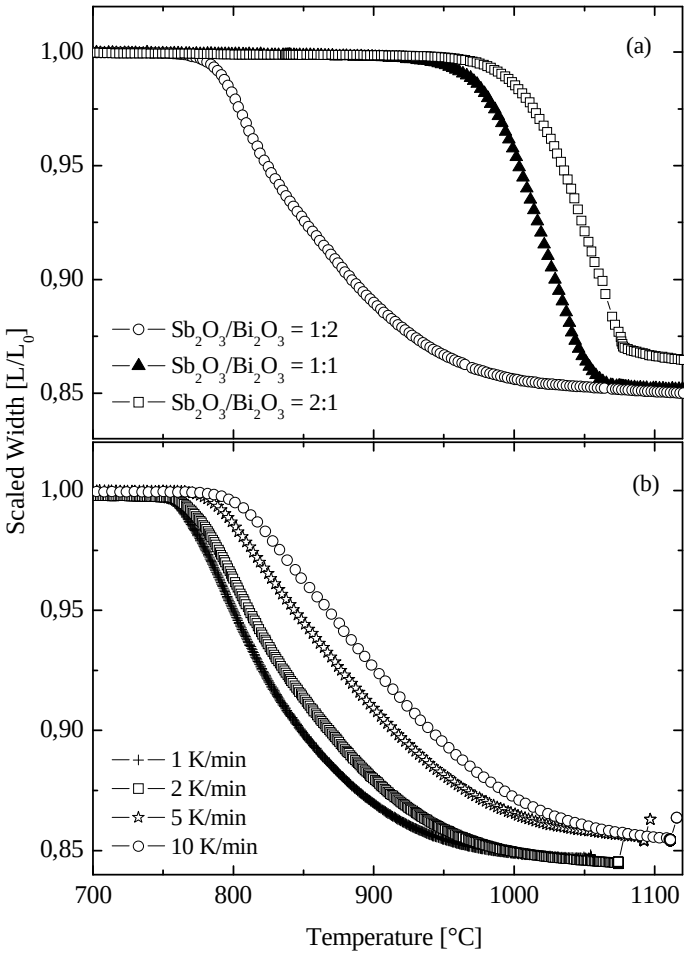

Figure 4.11: Shrinkage of ZBS green samples a) at a heating rate of 5 K/min with different Sb_2O_3/Bi_2O_3 ratios and b) at different heating rates and a constant Sb_2O_3/Bi_2O_3 ratio of 1:2

The T_{50} temperatures for the wet mixed and dry mixed powders at a heating rate of 5 K/min are 875 and 850 °C respectively. This small change of onset and T_{50} temperatures between dry- and wet-milled

samples indicates that sintering kinetics was essentially unaffected from details of the preparation process.

After the onset of sintering thermal diffusivity usually increases in ceramic green samples [53], i.e. temperature gradients are expected to decrease at constant heating rate. Therefore, the increasing differences between T_{50} temperatures and onset temperatures with increasing heating rate (compare table 4.3) were attributed to sintering kinetics and not to temperature gradients.

Table 4.3 T_{onset} and T_{50} values for milled and wet mixed samples

	1 K/min	2 K/min	5 K/min	10 K/min
T_{onset} (°C)	757	761	780	796
T_{50} (°C)	823	840	875	899

From the shrinkage data shown in Figure 4.11b kinetic field diagrams were constructed according to section 3.4.2. Kinetic field diagrams were plotted and compared directly to sintering models. The kinetic field diagrams are shown in figure 4.12.

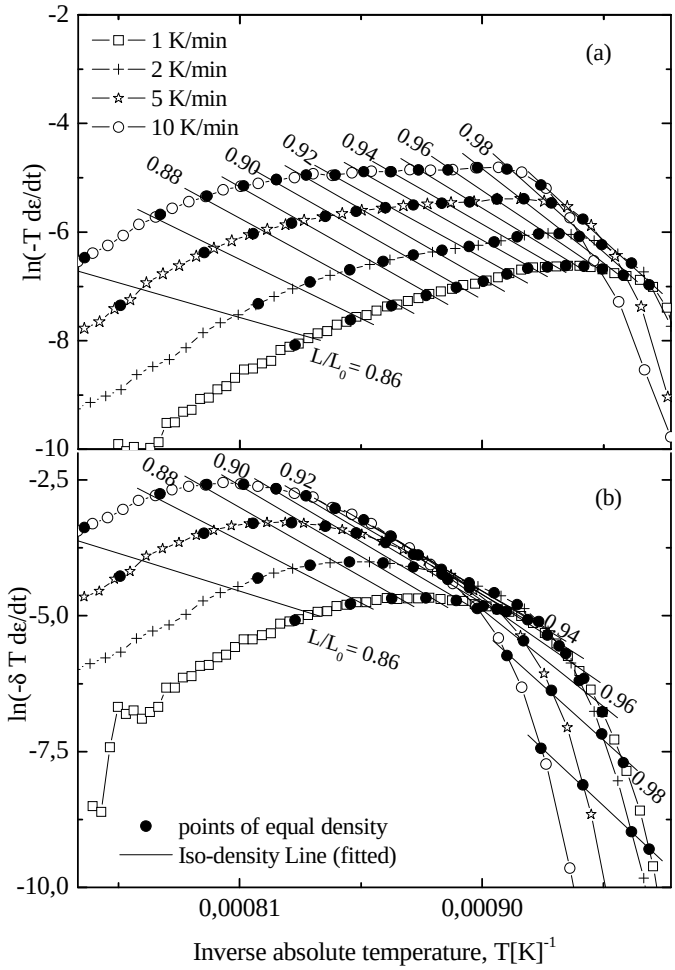

Figure 4.12: Kinetic field diagram of the data shown in Figure 4.11 with iso-strain lines: a) plotted in the standard way, b) plotted after transformation of y-axis according to equation 3.6

It can be seen that the iso-strain lines form straight lines. Due to the use of Arrhenius type diagram, the slope of these lines can be interpreted as apparent activation energy for densification (Figure 4.14). Since different mechanisms interact during densification, the apparent activation energy doesn't correspond to one specific mechanism [54].

Figure 4.14 shows that the apparent activation energy derived from the slope of the iso-strain lines did not change much with the transformation of the y-axis in the kinetic field diagram. But it is

evident from figure 4.12b that the iso-strain lines related to strain values between 0.96 and 0.91 are parallel and close to one single line. This suggests that – in this strain range -sintering kinetics is controlled completely by the right term: $E_D/(RT)$ in equation 3.6.

Equation 3.6 was fitted to the experimental iso-strain lines of Figure 4.12b using an in-house least square fitting software which was based on a gradient search algorithm. For that, the measured ZnO particle size of 1.56 micron was used as G_0 (see table 2.1). Different exponents for grain growth m and densification n between 3 and 6 were tested in the fits. The smallest χ^2 was obtained with n=3, m=3 respectively with n=4, m=4. In this range of exponents the quality of the fits was good and small differences in χ^2 were considered not significant. The fitted parameters are shown in table 4.4. The range indicates the variation of the respective parameters within the acceptable range of exponents. A kinetic field diagram obtained from the theoretical strain rate curves is shown in Figure 4.13. Good agreement to the experimental iso-strain lines was obtained.

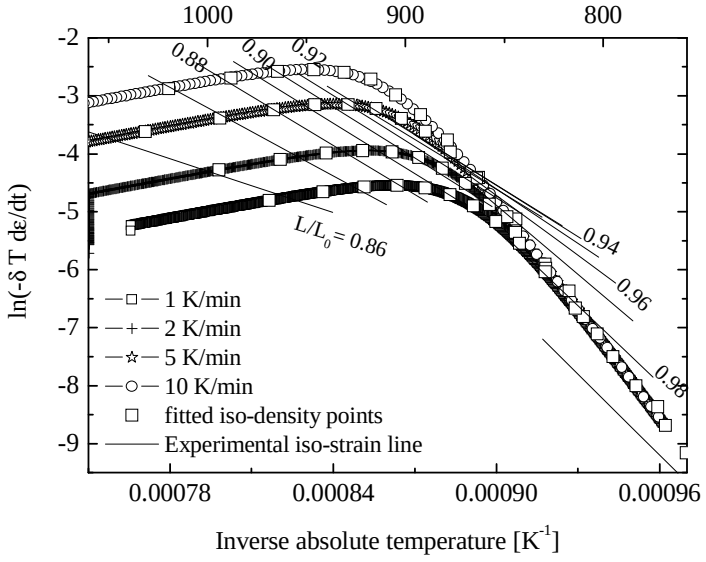

Figure 4.13: Kinetic Field diagram re-produced by fitting iso-density lines to equation 3.6 n=3 and m=4

Table 4.4 Fitted grain sizes of ZnO G_{ZnO} and activation energies for diffusion E_D respectively grain growth E_G during sintering of ZBS green samples at a heating rate of 10 K/min

Temperature [°C]	G_{ZnO} [µm]	E_D [kJ/mol]	E_G [kJ/mol]
800	1.65 – 1.65	500±20	570±10
900	2.13 – 2.74		
1000	6.22 – 7.30		
1100	13.25 -17.63		

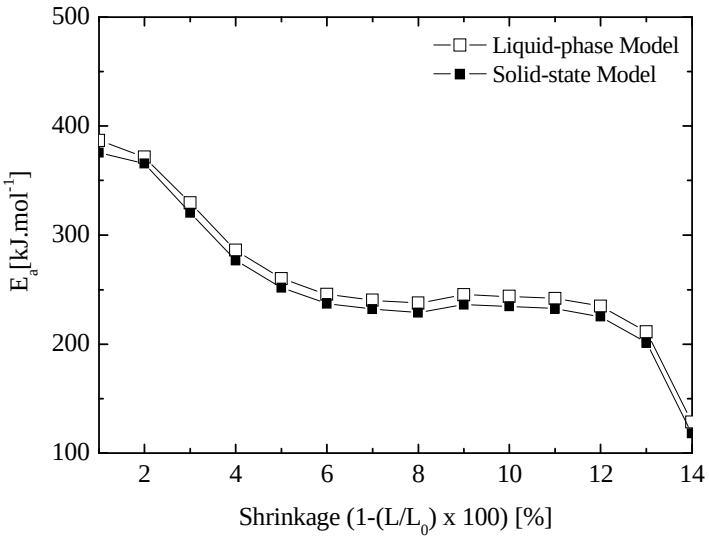

Figure 4.14: Apparent activation energy (E_a) as a function of linear shrinkage for ZBS sample using liquid-phase (top) and solid-state (bottom) equation of sintering

4.2.2 Microstructure analysis

To complement the findings from the kinetic field analysis the microstructure of partially sintered and quenched ZBS samples was investigated. Figure 4.15 shows SEM images of polished sections of green samples heated to different temperatures with a heating rate of 10 K/min. ZnO can be distinguished by its grey contrast from the

darker pores and a brighter inter-grain phase. The different constituents of the inter-grain phase (Bismuth oxide, pyrochlore, and spinel) were not distinguished. The average chord lengths of ZnO grains, pores and inter-grain phase were obtained from lineal intercept analysis of the SEM images (Figure 4.16a). A steep increase of ZnO grain size was measured between temperatures of 900 and 1000°C. The growth of ZnO grains was accompanied by a coarsening of pores and inter-grain phase, where the inter-grain phase showed smaller chord lengths compared to the pores at the respective temperature (compare Figure 4.16a).

The chord lengths of ZnO grains followed a log-normal distribution and hence average grain sizes were calculated using Mendelsons model (See section 3.3).

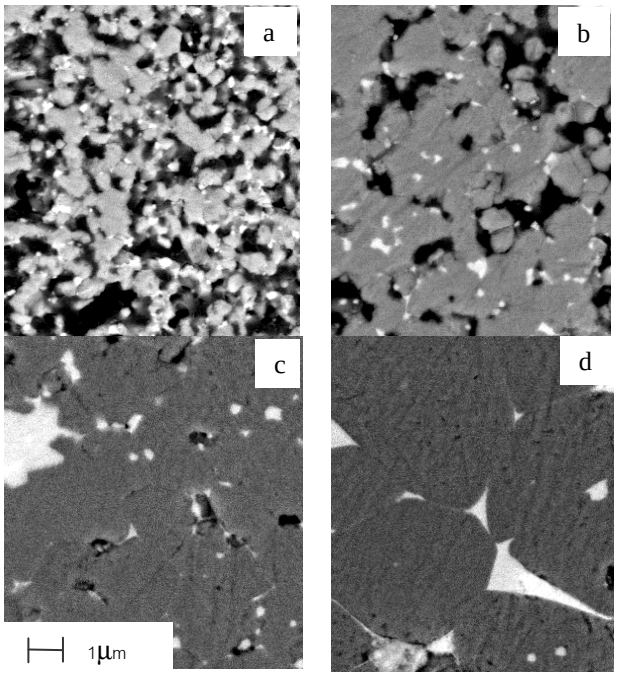

Figure 4.15 Backscattered electron micrographs of ZBS samples quenched into liquid Nitrogen from (a) 800-, (b) 900-, (c) 1000- and (d) 1100 °C

Figure 4.16b compares the ZnO grain sizes from the microstructure analysis with the grain size obtained from fitting equation 18 (see section 3.4.2) to the kinetic field data (compare table 4.4). A reasonable agreement between both methods was obtained. Note that the larger difference in the final sintering stage can be attributed to the limited scope of equation 3.6 which covers the intermediate sintering stage only.

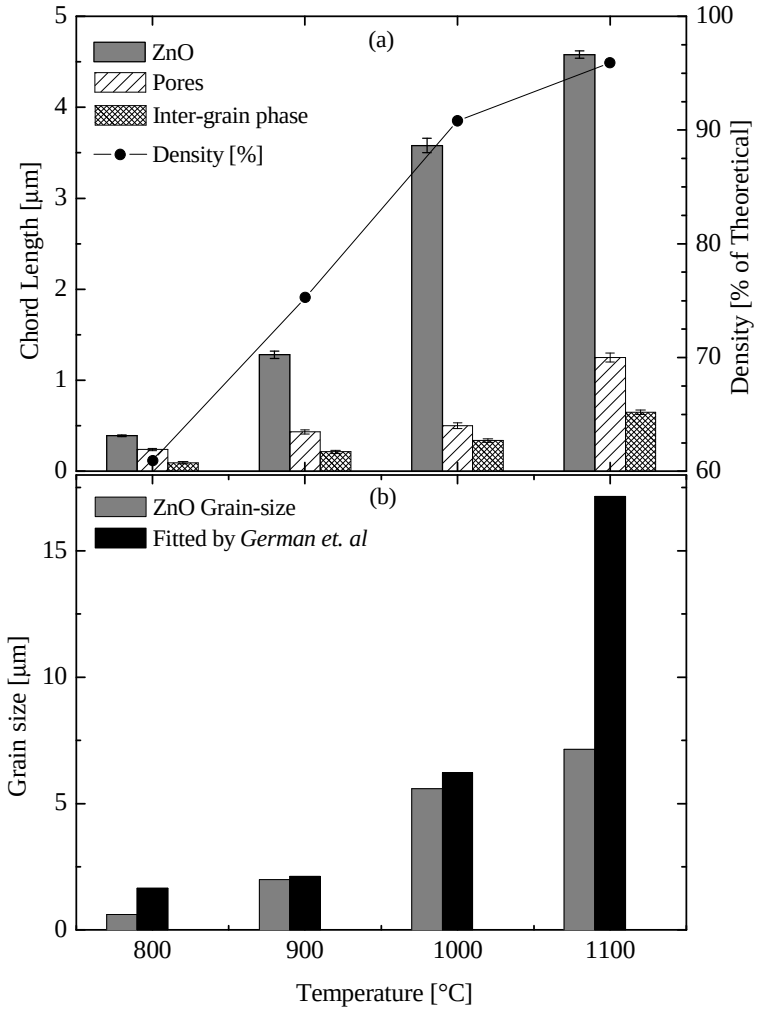

Figure 4.16 (a) Chord-lengths of ZnO-, liquid- and pore and (b) average grain sizes of ZnO from chord-length (grey) and by fitting (black) in the ZBS ceramic as function of quenching temperature. Corresponding density values obtained from optical dilatometry are also shown on the right-y axis of (a)

4.2.3 Wetting behaviour of the melt phase

Using the ternary mixture including Sb_2O_3 the melting was shifted to higher temperatures above 800°C compared to the binary mixture where it occurred close to the eutectic temperature of 738°C. Therefore, the wetting experiments were performed at two different temperatures. Figure 4.17 shows the contact angle after depositing a droplet of the binary or ternary mixture on the ZnO substrate. The contact angles were very small. They decreased slightly and approached 5° and 1° for the binary and ternary powder mixture after about 20 minutes.

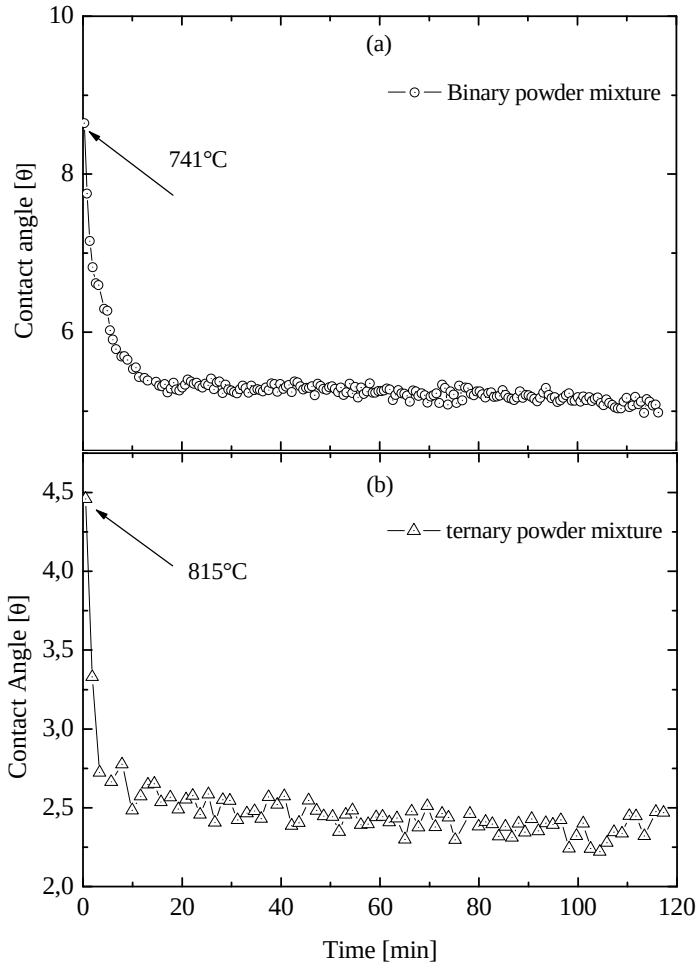

Figure 4.17: comparative wetting of pure ZnO substrate by - (a) binary (-o-) and (b) ternary (-Δ-) powder mixtures. Note that the melting points are different

4.2.4 Discussion

The large impact of the molar ratio of Sb_2O_3 and Bi_2O_3 on sintering kinetics shown in Figure 4.11a was already measured by other groups [18]. It was explained by the formation of solid pyrochlore ($Zn_2Bi_3Sb_3O_{14}$) which requires an equimolar ratio of both sesquioxides [18]. The 1:2 molar ratio of Sb_2O_3 and Bi_2O_3 allows for early melt formation from excess Bi_2O_3 which explains the low onset temperature of 760°C – only slightly above the eutectic temperature of 738°C in the binary ZnO-Bi_2O_3 system. An increase of melting temperature to 760°C was predicted from thermodynamic modelling for the ternary ZnO-Bi_2O_3-Sb_2O_4 system [49]. This increase was confirmed in the present study by the wetting experiments using binary and ternary mixtures of Bi_2O_3 and ZnO and Bi_2O_3, ZnO and Sb_2O_3 respectively. The increase of onset temperature with increasing heating rate (compare Figure 4.11b) was attributed to heat flow within the samples and initial local sintering after melt formation. Pyrochlore decomposes at a temperature around 1000°C and spinel ($Zn_7Sb_2O_{12}$) is formed [18]. Thereby Bi_2O_3 is released and sintering can proceed - also in the systems with molar ratios of Sb_2O_3 and Bi_2O_3 ≤ 1(compare Figure 4.11a).

The apparent activation energy for sintering of ZBS green samples, which was derived from the slope of the iso-strain lines, is in the range of 200 to 400 kJ/mol, decreasing during densification (compare Figure 4.14), is much smaller than the activation energy for diffusion of ZnO species in the melt phase of 500 kJ/mol (compare table 4.4) which was derived from the fit of equation 3.6 (section 3.4.2). The difference is explained by the counteraction of grain growth and diffusion with respect to densification. Both phenomena are thermally activated i.e., they show a strong increase with temperature, but the diffusion coefficient appears in the numerator whereas the grain size controls the denominator (compare equation 3.6). The activation

energy for grain growth of 580 kJ/mol is higher than the activation energy for diffusion. Therefore, the counteraction leads to an anticlockwise rotation of iso-strain lines with increasing density. This can be understood considering two points A and B on an iso-strain line in intermediate sintering stage (compare Figure 4.18). Point A is obtained from a sintering experiment with a low heating rate and point B from a sintering run with high heating rate. The temperature increase, which is required for a strain decrement $\Delta L/L_0$ to reach points A´ and B´ at the next iso-strain line, depends on grain growth. At the smaller heating rate grain growth rate is relatively smaller compared to diffusion rate because the temperatures are smaller than at the higher heating rate and the activation energy for grain growth was higher than the activation energy for diffusion. This means the distance A-A´ is smaller than the distance B-B´ which explains the anticlockwise rotation (compare Figure 4.18). Note, that a parallel shift of iso-strain lines is expected if $E_D=E_G$ and a clockwise rotation if $E_D>E_G$ [41].

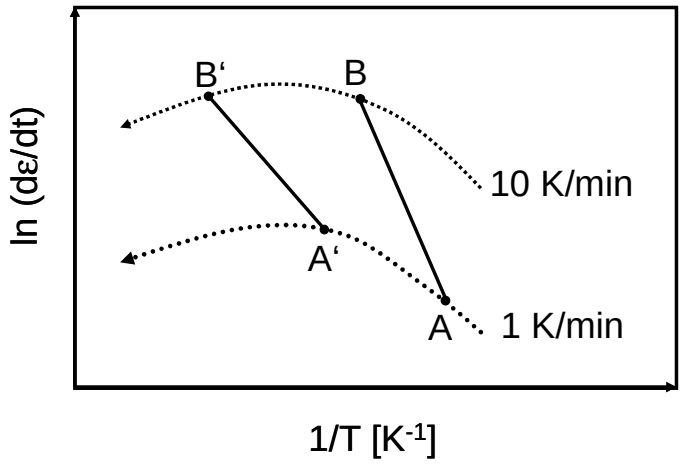

Fig 4.18 Schematic diagram showing rotation of iso-strain line AB when going to A´B´ in a kinetic field diagram ($E_G>E_D$ see text) [52]

The activation energy for grain growth of 580 kJ/mol is rather high compared to the activation energies presented by other groups (see

table 1.1 in section 1.4.2). It is assumed that this activation energy also reflects a mixture of different mechanisms. So the Zener drag process for spinel particles or pores at the ZnO grain boundary interferes with the growth process from Ostwald ripening. Presumably the Zener drag process and Ostwald ripening have different activation energies. The counterplay of the two mechanisms may lead to similar apparent activation energy for grain growth as it was described for densification in the previous paragraph.

The modified kinetic field shown in Figure 4.12b is considered superior compared to the standard kinetic field shown in Figure 4.12a in describing liquid phase sintering. The transformation of the y-axis according to liquid phase sintering models allows for a direct identification of grain growth. Grain growth leads to a shift of iso-strain lines to the left hand side in the kinetic field diagram because it increases the denominator in equation 3.6. This has to be compensated by an increased diffusion coefficient in the numerator which requires higher temperatures. From the modified kinetic field the onset of considerable grain growth can be directly recognized. In the present example this shift occurs at a strain of 0.9 (compare Figure 4.12b). At a heating rate of 10 K/min this strain corresponds to a temperature of 950°C (compare Figure 4.11b). It is in the temperature range of fast grain growth which was identified by microstructure analysis (compare Figure 4.16).

The magnitude of the shift of the iso-strain lines to the left hand side provides a measure for the grain growth rate which can be used in comparing sintering behaviour of different green samples. The change of the slope of the iso-strain lines, i.e. anticlockwise rotation in the present example using ZBS green samples, enables direct conclusions on the heating cycle required for a change in the grain size of dense samples. So for the ZBS samples it was reasoned that a longer holding period at lower temperatures leads to smaller grains at same density

than a shorter holding period at higher temperatures. It was reported for customary and nanocrystalline ZnO based varistor ceramics that a holding period at lower temperature indeed leads to a finer microstructure [50,51].

In the initial sintering stage the iso-strain lines shift to the right hand side. This can be seen for L/L_0=0.98, 0.96 and 0.94 in Figure 4.12b. It is not surprising that equation 18 cannot be applied in this stage because it was derived for intermediate stage sintering. But apart from this shift of iso-strain lines an intersection of strain rate curves in the low temperature regime is observed for both types of kinetic field diagrams (compare Figure 4.12a and b). Initially strain rates at lower heating rates are higher than at higher heating rates. In the intermediate sintering stage the usual relation between strain rates and heating rates is restored. A similar transposition in the initial sintering stage was not observed for solid state sintering processes (compare e.g. [41]). It was assumed that a slow mechanism, which is not affected much by temperature, retards densification in this stage. Such a mechanism could be the redistribution of liquid phase. The redistribution is controlled by wetting properties, and viscosity of the melt and pore size distribution of the compact. The contact angle experiments for the ZBS system had shown that the melt has good wetting behaviour. Also the viscosity of the melt is assumed to be small allowing a fast redistribution.

From the microstructure investigations it was observed that the melt fills part of the pores completely whereas other pores are filled completely by the vapour phase (compare figure 4.15). This separation of the two fluid phases is in contrast to theoretical liquid phase distributions reported in literature where the liquid is arranged around the particle contacts in the initial sintering stage [30]. It was assumed that the driving force for the separation is the liquid-vapour

interfacial energy. The liquid-vapour interface can be drastically reduced by the separation of both fluid phases.

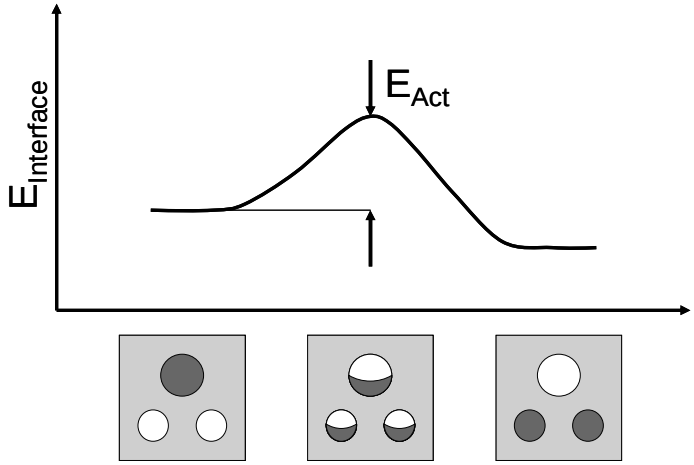

Figure 4.19 Interface energy during liquid redistribution - starting from a filled large pore and two empty smaller pores (left), versus partially filled pores (middle), and ending with an empty large pore and two filled smaller pores (right) [52]

The average chord length for the inter-grain phase was smaller than the average chord length of the pores (compare Figure 4.16a). This could be interpreted as a confirmation of the pore filling theory which claims a preferred filling of smaller pores by wetting melts during liquid phase sintering [55]. A thermodynamic justification was given for the pore filling theory considering the larger specific surface of smaller pores and corresponding larger decrease of interface energy by filling with the melt compared to the larger pores. However, in the present study a closer look to the microstructures showed that during the entire sintering cycle also large pores were filled by the liquid phase. This was explained by an energy barrier which prevents redistribution according to the thermodynamic minimum (Figure 4.19). The redistribution requires an intermediate state where pores are only partially filled. The additional liquid-vapour interface within these pores cost additional energy. So an activation energy exists

which hinders liquid redistribution according to the thermodynamic minimum.

Considering this energy barrier an initially inhomogeneous distribution of the melt phase leads to local shrinkage in the regions surrounding pores which are filled by the melt whereas no shrinkage occurs in other regions. After some shrinkage the local decrease of pore volume causes liquid flow to neighbouring regions which can subsequently sinter. Although this leads finally to high densification in all regions, a delay of shrinkage in the initial sintering stage is expected which is in agreement to the transposition of iso-strain lines observed in the present study. An inhomogeneous microstructure of the sintered ceramics can originate from this kinetic effect. E.g., grain growth is faster in regions which are already dense because the grain boundary mobility is not decreased by pores. In the ZBS system - at temperatures below 1000°C - an additional increase of local grain growth can be caused by the absence of spinel particles. It was concluded that the initial homogeneous distribution of Bi_2O_3 is essential to achieve a homogeneous microstructure of the sintered varistors.

4.3 Electrical Characterisation of ZnO-based varistors

4.3.1 Electrical (J-V) Characteristics

The MnO-doped samples were analysed for common electrical properties like non-linear exponent (α), break down field (E_b) and leakage current (J_L). Break down field was measured at a current density of 1 mA/cm^2 and current density is reported as J_L. The samples showed reasonable electrical responses in terms of α, E_b and J_L compared to commercial varistor ceramics which are doped with at least 15 different additive oxides to optimize for their aforementioned electrical properties.

Table 4.5. α, E_b and J_L for the ZBS samples doped with 0.5 mol% MnO (heating rate for all were 2 K/min)

Sb:Bi-ratio	α	E_b (Vmm^{-1}) (1 mA.cm^{-2})	Leakage current, J_L (A)
1:1	31.36	151.39	7.72 x 10^{-9}
1:2	30.52	122.15	4.09 x 10^{-8}
2:1	4.75	56.92	7.45 x 10^{-7}

Figure 4.20 shows field strength (V/mm) as functions of current density (A/cm^2) for MnO-doped samples. Two samples with Sb:Bi ratio of 1:1 and 1:2 showed reasonable J-V characteristics with an alpha value of 31 and 30 respectively and break-down field of 151- and 122 Vmm^{-1} respectively. For commercial compositions of ZnO-based varistors the values for α and E_b parameters are acceptable to be around 50 and 210 Vmm^{-1} respectively. Also the leakage current found to be in the nano- and/or near nano Ampere range. The values are shown in table 4.5.

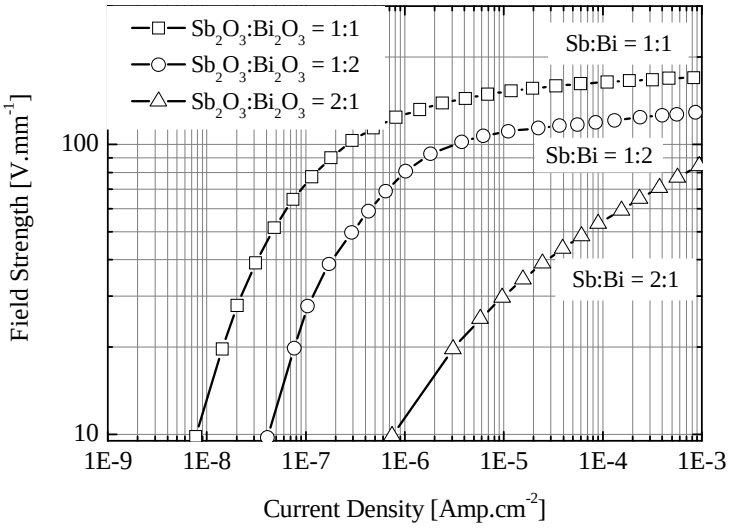

Figure 4.20 Current-density versus field-strength (J – V) characteristic of MnO-doped ZBS samples with different ratios of Sb_2O_3 and Bi_2O_3

However, the sample with Sb:Bi ratio of 2:1 showed a different characteristic compared to the other two samples. Both α and E_b values were unexpectedly low – around 5 and 57 Vmm^{-1} respectively. Amount of leakage current was also very high indicating a considerable amount of current-flow through the varistor.

On the other hand, non-doped samples showed expected values for all of the aforementioned parameters which seen to have been little influenced by the rate of heating. The ratios between Sb_2O_3 and Bi_2O_3 in these samples were maintained constantly at 1:2. Table 4.6 shows the accumulated values for these parameters in non-doped samples.

Table 4.6 α, E_b and J_L for the ZBS samples without MnO doping (fixed Sb:Bi ratio of 1:2)

Heating rate (K/min)	α	E_b (Vmm^{-1}) (1 $mA.cm^{-2}$)	Leakage current (A)
1	7.84	-	3.02×10^{-8}
2	8.12	61.55	1.02×10^{-7}
5	8.89	54.61	1.58×10^{-8}
10	8.12	59.43	3.47×10^{-8}

If we compare the sample sintered at 2 K/min in table 3 to the one with Sb:Bi = 1:2 in table 2 then the large difference in their electrical properties is clearly made by the doping of MnO.

However, the electrical property of the Sb:Bi = 2:1 ratio sample of table 4.5 is surprisingly different from other doped samples and unexpectedly similar to those of the non-doped samples.

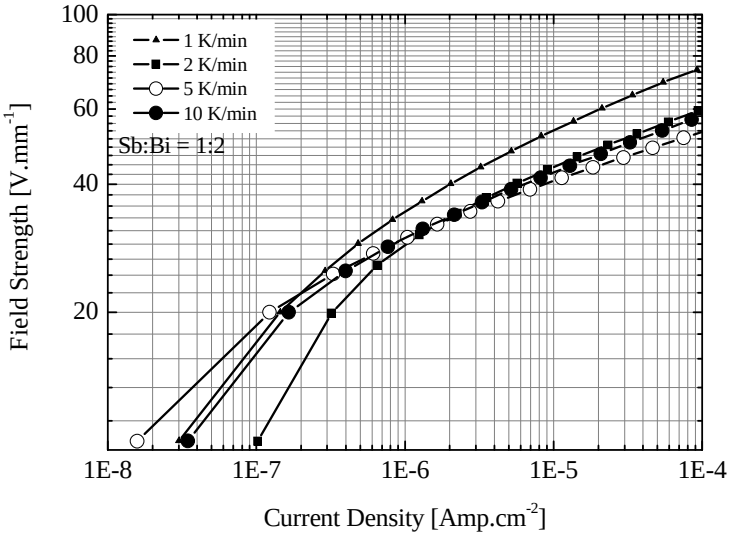

Figure 4.21 Current-density versus field-strength (J – V) characteristic of non-doped ZBS samples with Sb_2O_3: Bi_2O_3 = 1:2 sintered at 1-, 2-, 5- and 10 K/min

To be able to explain this strange behaviour room temperature XRD analysis of all the samples were done.

4.3.2 Room Temperature Phase analysis

Room temperature XRD analysis gave us some important phase information which was helpful to explain the electrical behaviour of the doped and non-doped samples. The XRD data were evaluated according to section 3.1. Bar diagram of scaled areas under pyrochlore-, Spinel- and Bi_2O_3 peaks is shown in figure 4.22. Amount of free crystalline Bi_2O_3 reduced with MnO-doping and the reduction was more prominent for samples with higher Sb_2O_3 content (compare figure 4.22). However, amount of pyrochlore seen was lowest for the non-doped sample.

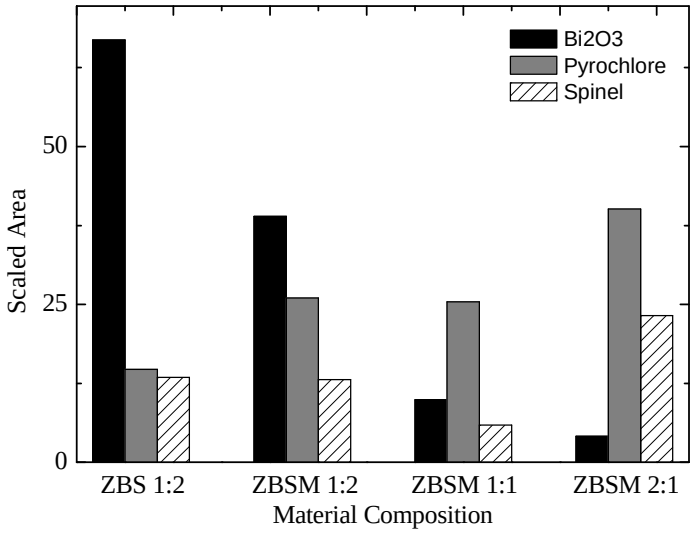

Figure 4.22 Bar-diagram showing scaled-areas under the Bi_2O_3, pyrochlore and spinel peaks obtained from room temperature XRD analysis of different samples with (ZBSM)- and without (ZBS) MnO-doping

Figure 4.23 shows the second half of the spectra with higher diffraction angles where we can see typical phases like pyrochlore, two different kinds of spinels (Zn-Sb-spinel, Zn-Sb-Co-spinel), ZnO and Bi_2O_3. It should be noted that although we doped the samples with MnO, our matched peaks showed traces of Zn-Sb-Co-spinel or $(Zn_{0.6}Co_{0.4})(Co_{1.33}Sb_{0.67})O_4$ (compare figure 4.23) which has the same structure (FCC) as Zn-Sb-Mn-spinel. The XRD analyses suggest that amount of pyrochlore increased with MnO-doping and the increase was higher for higher Sb-content of the sample. So, more MnO and Bi_2O_3 were consumed by pyrochlore and thus a depletion of MnO and/or Bi_2O_3 was caused at the grain boundaries which actually offer the characteristic non-linearity in varistor. This can be cross-checked by the fact that both pyrochlore and spinel peaks changed their positions in the doped samples (compare figure 4.23) with respect to the non-doped samples. This explains why we had lowest non-linearity coefficient for the sample with Sb:Bi = 2:1 even though it was

doped with MnO. Leakage current also increased with higher Sb-content (table 4.4).

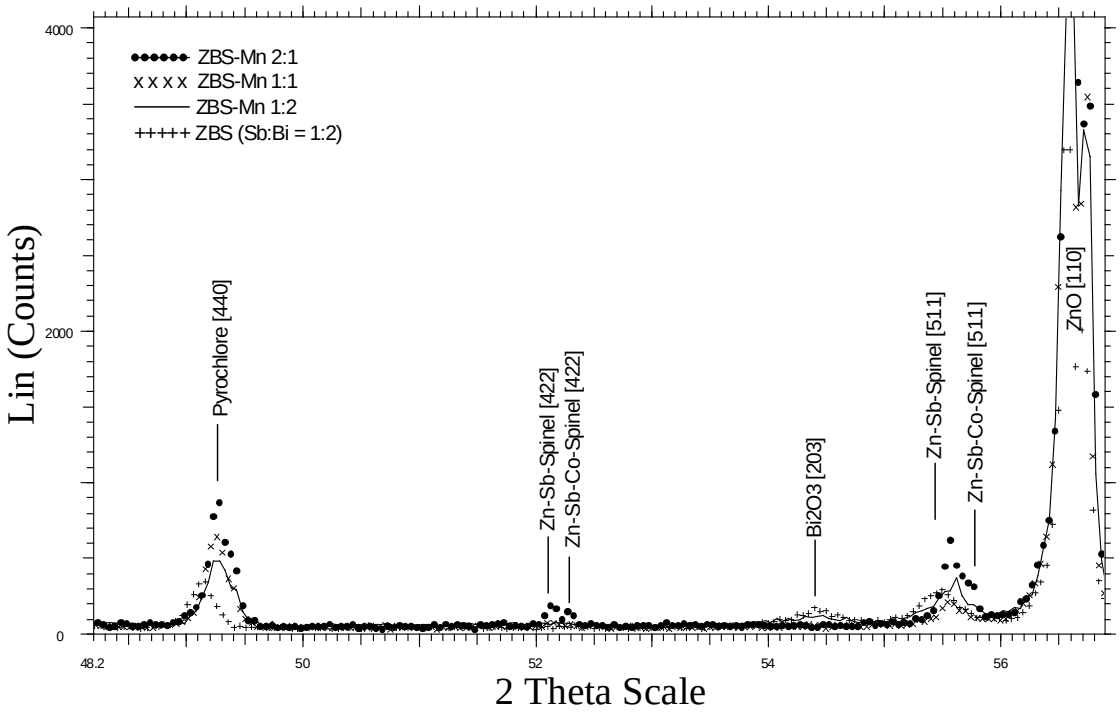

Figure 4.23 Room-temperature XRD analysis of the doped and non-doped varistors showing important phases like Bi_2O_3, pyrochlore, spinel and ZnO. Shift of the pyrochlore and spinel peaks are also noticeable.

Chapter 5: Conclusions

Several techniques were used in the current study to realize the observation and optimization of the liquid-phase sintering phenomenon. The objective was to learn about phase evolution, sintering kinetics, thermodynamic equilibriums and finally electrical characterisation of the ternary ZBS sample. This includes X-ray diffraction experiments using high temperature and high energy synchrotron radiation at Hasylab (Hamburger Synchrotron Laboratory), in-situ optical dilatometry using an optical dilatometer, thermodynamic simulations using Factsage and Theriak-Domino simulation-packages and finally characterisation of the doped (with MnO)- and non-doped ZBS samples at the scientific facility of ABB-Switzerland.

5.1 High Temperature XRD analysis

Phase formation during sintering of ZBS was measured in situ, using 1 mm thick samples and synchrotron X-rays. Sintering shrinkage was measured in different atmospheres by an optical method. Thermodynamic calculations were useful to explain phase formation, composition, stability of additive oxides and influence of the oxygen fugacity on sintering. Sb_2O_4, pyrochlore, trirutile and spinel were formed at temperatures of 500°C to 800°C. The oxidation of antimony was controlled by the oxygen partial pressure and affected both, phase formation and sintering kinetics, in the ZBS system.

The control of oxygen activity in the furnace atmosphere during sintering of ZBS is required to avoid variations in the oxidation state of antimony. It was shown that sintering kinetics is strongly affected by the presence of Sb_2O_4 and Sb_2O_3 respectively. With increasing partial pressure of oxygen, Sb_2O_4 becomes stable. Its refractory

character can help to minimize vapour loss and shift the melt formation to higher temperatures.

5.2 Kinetic Field analysis by Optical dilatometer

A modified kinetic field technique was applied to analyze liquid phase sintering. It was based on general liquid phase sintering models for Ostwald ripening and contacts flattening. From the new approach one could estimate microstructural changes during sintering. Any indication of grain growth during sintering can be understood indirectly by the shift of the iso-strain lines to the left hand side on a kinetic field diagram. Also the magnitude of such shifts can provide with the measure of grain growths. It was found previously [50,51] that a holding period at lower temperature during sintering of customary and nano crystalline ZnO based ceramics can result in finer microstructure. Now this conclusion was directly obtained from the change of slope of the iso-strain lines in the modified kinetic field diagram. Although mathematical simulations and microstructure analysis were done to complement our findings it is emphasised that, neither microstructure analysis nor mathematical fitting is required to make decision on heating cycles for a liquid phase sintering of particular sample or compare sintering activities of different green bodies. This is considered the most important result for practical applications because it enables an efficient optimization of the manufacturing process using basically 4 sintering runs per type of green sample and the construction of the respective kinetic field diagram.

5.3 Electrical characterisation

In conclusion, we have compared electrical properties of three MnO-doped varistor ceramics based on ZnO and tried to explain how doping affects the micro-varistor configuration by modifying its phase

compositions. MnO is well-known for its influence on the non-linearity of the ZnO varistors [5]. The experiments also showed the improvement in the non-linearity of current-voltage behaviour for the doped samples. However, the electrical properties are satisfactory owing to the fact that they were not doped with as many as 15 different additives like the commercial ones. With this limitation in mind the doped samples showed promising non-linearity, energy consumption ability and acceptable leakage-current, showing that they can be used as model system for sintering of ZnO based varistor ceramics.

5.4 Outlook

As for now, a kinetic field analysis of the intermediate stage of liquid-phase sintering is done; but a complete three-stage kinetic field can be established to increase the control on the liquid-phase sintering in the future. Relations between microstructural grain-growth, diffusion and activation energy were already clear from the current kinetic field which indicate that, a complete three-phase kinetic field will be able to predict the entire heating cycle of sintering.

Our thermodynamic simulations also leave the opportunity to concentrate more on the ternary ZBS system so that a real three-component (ZnO, Bi_2O_3 and Sb_2O_3) thermodynamic model can be developed and the stability of different phases can be realised from a more practical viewpoint.

References

1. Bradt R. C. and Susan L. Burkett, Microstructural control of Zinc Oxide Varistor ceramics, *"Ceramic Microstructures – Control at the Atomic Level"*, Book by Antoni P. Tomsia, Andreas M. Glaeser, P 339-348

2. Matsoka M., Nonohmic Properties of Zinc Oxide Ceramics, Jpn. J. Appl. Phys. **10** (1971), 736 - 746

3. Guha J. P., kunej S. and Suvorov D.: Phase equilibrium relations in the binary system Bi_2O_3-ZnO, J. Mat. Sci. 39, 911 - 918 (2004)

4. Clarke David R., Varistor Ceramics, J. Am. Ceram. Soc., 82 [3] 485-502 (1999)

5. Inada M., Crystal Phases of Nonohmic Zinc Oxide Ceramics, Jpn. J. App. Phys. **17**(1978), No. 1, 1-10

6. Kumari K. G. Vasantha, Vasu P. Divya, Kumar Viswanathan, Asokan Thangavelu and Davies P. K., Formation of Zinc–Antimony-Based Spinel Phases, J. Am. Ceram. Soc. 85 (2001), 703-705

7. Morris W.G., Physical properties of the electrical barriers in varistors, J. Vac. Sci. Technol., 13, 926-931 (1976)

8. Olsson E. and Dunlop G.L., Characterization of Individual Intetfacial Barriers in a ZnO Varistor Material, J. Appl. Phys., 66, 3666-75 (1989)

9. L Levinson. M. and Philipp H. R., "Zinc oxide varistors - a review", Amer. Cer. Soc. Bull. 65 (4), 639 (1986)

10. Wong J., Microstructure and phase transformation in a highly non-ohmic metal oxide varistor ceramic, J. App. Phys. **46** (1975), No. 4, 1653-1659

11. Inada M., Formation Mechanism of Nonohmic Zinc Oxide Ceramics, Jpn. J. App. Phys. vol. **19** (1980), No. 3, 409-419

12. Leite E. R., Nobre M. A. L., Longo E., Varela J. A., Microstructural development of ZnO varistor during reactive liquid phase sintering, Journal of Mat Sci. **31** (1996), 5391-5398

13. Kim J., Kimura T. and Yamaguchi T., Sintering of Sb_2O_3-doped ZnO, Journal of Materials Science **24** (1989), 213-219

14. Ott J., Lorentz A., Harrier M., Preissner E. A., Hesse C., Feitz A., Whitehead A. H., and Schreiber M., The influence of Bi_2O_3 and Sb_2O_3 on the electrical properties of ZnO-based varistors, Journal of Electroceramics **6** (2001), 135 – 146

15. Mahan G.D., Levinson L. M. and Philipp H. R.., Theory of conduction in ZnO varistors, J. Appl. Phys. 50 (1979) 2799

16. Wang H. and Chiang Y. M., J. Am. Ceram. Soc., 81, 89 (1998)

17. Mergen A. and Lee W.E., J. Europ. Ceram. Soc., 17, 1409 (1997)

18. Kim Jinho, Kimura Toshio, and Yamaguchi Takashi, Sintering of Zinc Oxide Doped with Antimony Oxide and Bismuth Oxide, J. Am. Ceram. Soc. **72** (1989), 1390-95

19. Kim Jinho, Kimura Toshio, and Yamaguchi Takashi, Effect of Bismuth Oxide Content on the Sintering of Zinc Oxide, J. Am. Ceram. Soc. **72** [8] (1989), 1541-44

20. Lao Yeh-Wu, Kuo Shu-Ting and Tuan Wei-Hsing, Effect of Bi2O3 and Sb2O3 on the grain size distribution of ZnO, J. Electroceramics, 19, (2007), 187-194

21. Oniyama E., Wahlbeck P. G., Phase Equilibria in the Bismuth-Oxygen System, J. Phys. Chem. B 102, (1998), 4418 – 4425

22. Wang H. and Chiang Yet-Ming, Thermodynamic Stability of Intergranular Amorphous Films in Bismuth-Doped Zinc Oxide, J. Am. Ceram. Soc., 81 [1], (1998), 89-96

23. Asryan N.A., Alikhanyan A.S. and Nipan G.D., Specifics of Sublimation of Antimony Oxides, Doklady Physical Chemistry, 392 [1-3], (2003), 221-226

24. Asryan N.A., Alikhanyan A.S. and Nipan G.D., Thermodynamic Stability of Antimony Oxides, Russian Journal of Physical Chemistry, 78 [1], (2004), 5-11

25. Guha J.P, Kunej Š. and Suvorov D., Phase equilibrium relations in the binary system Bi_2O_3-ZnO, J. Mat, Sci., 39 (2004), 911-918

26. Serena S., De La Rubia M.A., Caballero A.C. and Caballero Y.A., Thermodynamic study of the rich-Bi_2O_3 region of the Bi_2O_3-ZnO system, Bol. Soc. Esp. Ceram., 45 [3], (2006), 150-153

27. Rahaman M.N., Sintering of Ceramics, Published by CRC Press, 2007, Original from the University of Michigan, ISBN 0849372860, 9780849372865

28. Chow T. S., Wetting of rough surfaces, *J. Phys.: Condens. Matter, 10 L445-L451 (1998)*

29. Kingery, W.D., Densification during Sintering in the Presence of a Liquid Phase. I. Theory, J. Appl. Phys. 30, 301, 1959

30. German, R.M., Sintering Theory and Practice, Wiley, New York, 1996

31. Bale C. W., Chartrand P., Degterov S. A., Eriksson G., Hack K., Ben Mahfoud R., Melancon J., Pelton A. D., Petersen S., FactSage thermochemical software and databases. – CALPHAD **26** (2002), 189-228

32. Takemura T., Kobayashi M., Takada Y. and Sato K., High Temperature X-Ray Diffraction Measurements of ZnO Varistor Ceramics, Jpn. J. Appl. Phys. **25** (1986), No.2, 295-296

33. Hubell J. H., Seltzer S.M., Tables of X-Ray Mass Attenuation Coefficients and Mass Energy-Absorption Coefficients, National Institute of Standards and Technology, Gaithersburg, Maryland; /physics.nist.gov/PhysRefData/XrayMassCoef

34. Senda T. and Bradt R.C., "Grain growth in ZnO and ZnO-Bi_2O_3 ceramics", J. Am. Ceram. Soc. 73 (1), 106 (1990)

35. Dey D. and Bradt R.C., "Grain Growth of ZnO during Liquid Phase Sintering", J. Am. Ceram. Soc. 75(9), 2529-34 (1992)

36. Senda T. and Bradt R.C., “Grain growth of Zinc Oxide during the sintering of Zinc Oxide-Antimony Oxide ceramics”, J. Am. Ceram. Soc. 74 (6), 1296 (1991)

37. Nunes Silvia Irene, Grain Growth of ZnO in ZnO-Bi_2O_3 Ceramics with Al_2O_3 Additions, J. Am. Ceram. SOC., 18 [9] 2469-75 (1995)

38. Suzuki Hironori and Bradt Richard C., Grain Growth in ZnO in ZnO-Bi_2O_3 Ceramics with TiO_2 Additions, J. Am. Ceram. SOC., 78 [5] 1354-60 (1995)

39. Chen Ying-Chung, Shen Chi-Yen and Wu Long, Grain growth processes in ZnO varistors with various valence states of manganese and cobalt, J.Appl.Phys.,Vol.69,No.12,15June 1991

40. Birnboim A., Gershon D., Calame J., Birman A., Carmel Y., Rodgers J., Levush B., Bykov Y. V., Eremeev A. G., Holoptset V. V., Semenov V. E., Dadon D., Martin P. L. and Rosen M., Comparative Study of Microwave Sintering of Zinc Oxide at 2.45, 30, and 83 GHz, J. Am. Ceram. Soc. 81 (1998) 1493

41. Raether, F., Schulze Horn, P..: Investigation of sintering mechanism of alumina using kinetic field and master sintering diagrams. To be published, J. Eur. Ceramic Soc. (2009)

42. Bernd Kämpfe, Falk Luczak, Bernd Michel, Energy Dispersive X-RayDiffraction, Part. Part. Syst. Charact. *22* (2005) 391–396

43. Risold D., Hallstedt B., Gauckler L. J., Lukas H. L., Fries S. G., The Bi-O system, J. Phase Equil. **16** (1995), 223-234

44. de Capitani C., Brown T. H., The computation of chemical equilibrium in complex systems containing non-ideal solutions, Geochim. Cosmochim. Acta **51** (1987), 2639-2652

45. Mendelson M.I., , Average Grain Size in Polycrystalline Ceramics, J. Am. Ceram. Soc., 52, [8] (1969)

46. Trontelj M. and Kraševec V., Effects of Antimony Oxide in the Sintering of ZnO Varistors, Advances in Varistor Technology, Edited by Lionel M. Levinson, J. Am. Ceram. Soc. **3**, 108-116

47. Werner G., Freiberg B., Reetz T. and Hilarius V., Particle growth in ZnO Powder, Proc. of the 3rd intl. Conf of the Europ. Ceram. Soc. Madrid, Spain (1993), 827-832

48. Palmour H. III, "Rate-controlled sintering technology for PM and composites". Powder Metal Report **9** (1988) 572

49. Arefin M.L., F. Raether, D. Doleijš and A. Klimera, Experimental study of phase formation during liquid phase sintering of ZnO ceramics, submitted at the Ceram. Int. (2009)

50. Balzer, B., Hagemeister, M., Kocher, P., Gauckler, L. J., Mechanical strength and microstructure of zinc oxide varistor ceramics; J. Am. Ceram. Soc., 87 (2004) 1932-1938

51. Duran, P., Tartaj, J., Moure, C., Fully dense, fine-grained, doped zinc oxide varistors with improved nonlinear properties by thermal processing optimization. J. Am. Ceram. Soc., 86 (2003) 1326-1329

52. Raether F. and Arefin L.M., Kinetic field approach to study liquid phase sintering of ZnO based ceramics, submitted to the J. Am. Ceram. Soc. 2009

53. Raether, F., Springer, R.: In-Situ measurement of neck formation during sintering of alumina by a novel thermooptical measuring device. Adv. Eng. Mat., 2 (2000) 741-744

54. Raether, F., Current state of in-situ measuring methods for the control of firing processes. J. Am. Ceram. Soc. 92 (2009) 146-152

55. Kim Y.-P., Jung, S.-W., Kang, S.-J. L., Enhanced Densification of Liquid-Phase-Sintered WC–Co by Use of Coarse WC Powder - Experimental Support for the Pore-Filling Theory. J. Am. Ceram. Soc., 88 (2005) 2106–2109

56. Beam line F3: http://hasylab.desy.de/facilities/doris_iii/beamlines/e35190/index_eng.html